

**Cotton Valley Fracture Imaging Project**  
**Phase III**

JIP Consortium

Well CGU 22-9

Carthage Field

Cotton Valley Formation

Carthage, Texas

April 1998 - May 1999

**Final Report Date:** July 9, 1999

# **Cotton Valley Fracture Imaging Project Phase III**

## **Final Report for JIP Consortium**

**Report Date: July 9, 1999**

By

Pinnacle Technologies, Inc.  
600 Townsend St., Suite 160W  
San Francisco, CA 94103

### **DISCLAIMER**

Neither Pinnacle Technologies, Inc. nor any person acting on behalf of Pinnacle:

- Makes any warranty or representation, express or implied, with respect to the accuracy, completeness, or usefulness of the information contained in this report, or that the use of any apparatus, method, or process disclosed in this report may not infringe privately owned rights; or
- Assumes any liability with respect to the use of, or for damages resulting from the use of, any information, apparatus, method, or process disclosed in this report.

---

# TABLE OF CONTENTS

TABLE OF CONTENTS .....	III
LIST OF FIGURES .....	IV
1. SUMMARY .....	6
2. DOWNHOLE TILTMETER ANALYSIS.....	13
2.1 DISCUSSION OF ERROR BOUNDS .....	16
2.2 LATERAL FRACTURE GROWTH ASYMMETRY .....	17
3. STRESS TESTING .....	21
3.1.1 Stress Test #1 – Bossier Shale (9,688’-9,690’).....	24
3.1.2 Stress Test #2 – C-Lime (9,458’-9,460’).....	33
3.1.3 Stress Test #3 – Sexton Shale (9,318’-9,320’).....	35
3.1.4 Stress Test #4 – Davis (shale-sand sequence) (8,862’-8,864’).....	38
4. WELL TESTING .....	41
5. PRODUCTION LOG RESULTS.....	43
6. FRACTURE MODELING .....	44
APPENDIX A – OVERVIEW OF DOWNHOLE TILTMETER FRACTURE MAPPING.....	56
APPENDIX B. HIGH DOWNHOLE TEMPERATURES AND THE IMPACT ON DOWNHOLE TILTMETER FRACTURE MAPPING .....	58
APPENDIX C. USE OF WELL TESTING DIAGNOSTIC PLOTS TO DETERMINE FRACTURE CLOSURE PRESSURE .....	59
APPENDIX D. RA-TRACER LOG AND PRODUCTION LOG.....	62
APPENDIX E. WELL LOG CGU 22-9 .....	63

---

# List of Figures

Figure 1. Plan view of hydraulic fracture azimuth and length in Well CGU 22-9 illustrating positions of the treatment well and the two observation wells. Lateral asymmetry in the growth of the Stage 4 fracture is clearly evident with roughly 2/3 of the growth occurring to the NE towards observation well CGU 20-6 (red line). .....	7
Figure 2. Stage 4 fracture geometry from DH-tiltmeter mapping .....	8
Figure 3. Fracture geometries from fracture modeling, downhole tiltmeter mapping and radioactive tracers for all 4 stages in the CGU 22-9.....	10
Figure 4. Stress profile with locations of stress tests and minifrac in the CGU 22-9 .....	11
Figure 5. Map view of treated well CGU 22-9, observation wells CGU 22-4 and CGU 20-6, and the fracture half-length and azimuth for Stage 4 downhole tiltmeter fracture mapping results. ....	14
Figure 6. Sensitivity of tilt magnitude as fracture grows towards an observation well .....	15
Figure 7. Fracture profile for Stage 4 in the CGU 22-9 well illustrating fracture size, target zone coverage, and significant lateral growth asymmetry.....	15
Figure 8. Theoretical error as a function of fracture height and half-length values. Crosshairs mark parameter values producing best match between actual and theoretical tiltmeter responses. White contour defines the resolution limit boundary around the solution point. ....	16
Figure 9. Theoretical, actual, and ideal tilt responses for each tiltmeter array in Stage 4 of well CGU 22-9 when allowing for asymmetric fracture growth. Note closer agreement between theoretical and ideal tilt responses in observation well CGU 20-6 when fracture is shifted approximately 200' to the NE as shown here.....	18
Figure 10. Theoretical, actual, and ideal tilt responses for each tiltmeter array in Stage 4 of well CGU 22-9 when assuming symmetric fracture growth. Note larger tilt responses for instruments within the array located at observation well CGU 20-6. A fracture with lateral symmetry would produce tilt magnitudes that are smaller than the measured ones in the CGU 20-6. ....	19
Figure 11. Error plot illustrating fracture lateral asymmetry. Fracture center (blue triangle at bottom of curve) has shifted approximately 200 feet along the fracture azimuth away from the wellbore to the NE. Yellow region at bottom of curve defines the resolution limits of the analysis.....	20
Figure 12. Measured stress profile in the CGU 22-9 .....	22
Figure 13. Wellbore configuration: CGU 22-9 .....	23
Figure 14. Stress Test #1 injection history.....	25
Figure 15. Injection #1: Pressure falloff with flow pulse shows closed fracture.....	26
Figure 16. Injection #1: Log-log diagnostic plot of pressure decline .....	26
Figure 17. Injection #1: Leakoff-normalized diagnostic plot.....	27
Figure 18. Injection #2: Pressure falloff with flow pulses shows closed fracture .....	28
Figure 19. Injection #3: Log-log diagnostic plot of pressure decline .....	29
Figure 20. Injection #3: Leakoff-normalized diagnostic plot.....	29
Figure 21. Injection #4: Pressure falloff with flow pulses shows closed fracture .....	30
Figure 22. Injection #5: Log-log diagnostic plot of pressure decline .....	31
Figure 23. Injection #5: Leakoff-normalized diagnostic plot.....	31
Figure 24. Injection #6: Log-log diagnostic plot of pressure decline .....	32
Figure 25. Injection #6: Leakoff-normalized diagnostic plot.....	33
Figure 26. Stress Test #2 injection history.....	34
Figure 27. Stress Test #2 - Injection #1: Log-log diagnostic plot of pressure decline.....	35
Figure 28. Stress Test #3 injection history.....	36
Figure 29. Stress Test #3 - Injection #1: Log-log diagnostic plot of pressure decline.....	37
Figure 30. Stress Test #3 - Injection #1: Leakoff-normalized diagnostic plot.....	37
Figure 31. Stress Test #3 - Injection #1: Square-root of time plot to determine closure pressure.....	38
Figure 32. Stress Test #4 injection history.....	39
Figure 33. Stress Test #4 - Injection #2: Log-log diagnostic plot of pressure decline.....	40
Figure 34. Stress Test #4 - Injection #3: Log-log diagnostic plot of pressure decline.....	40
Figure 35. Postfrac pressure buildup test for Stage 1 – Taylor Sand.....	41

Figure 36. Postfrac pressure buildup test for Stage 2 – Roseberry/Ardis Sands .....	42
Figure 37. Treatment data: CGU 22-9 Stage 1 .....	46
Figure 38. Net Pressure Match: CGU 22-9 Stage 1 .....	46
Figure 39. Fracture Geometry: CGU 22-9 Stage 1 .....	47
Figure 40. Estimating closure pressure from log-log diagnostic plot: Stage 1.....	47
Figure 41. Estimate of closure from pump-in/flowback test confirms log-log plot estimates: Stage 1 .....	48
Figure 42. Treatment data: CGU 22-9 Stage 2 .....	49
Figure 43. Net Pressure Match: CGU 22-9 Stage 2.....	49
Figure 44. Fracture Geometry: CGU 22-9 Stage 2 .....	50
Figure 45. Estimating closure pressure from log-log diagnostic plot: Stage 2.....	50
Figure 46. Estimating closure pressure from square-root of time plot: Stage 2 .....	51
Figure 47. Treatment data: CGU 22-9 Stage 3 .....	52
Figure 48. Net Pressure Match: CGU 22-9 Stage 3 .....	52
Figure 49. Fracture Geometry: CGU 22-9 Stage 3 .....	53
Figure 50. Estimating closure pressure from square-root of time plot: Stage 3.....	53
Figure 51. Treatment data: CGU 22-9 Stage 4 .....	54
Figure 52. Net Pressure Match: CGU 22-9 Stage 4.....	54
Figure 53. Fracture Geometry: CGU 22-9 Stage 4 .....	55
Figure 54. Estimating closure pressure from log-log diagnostic plot: Stage 4.....	55
Figure 55: Theoretical deformation pattern from downhole tiltmeters during a fracture treatment. ....	56
Figure 56. Examples of raw downhole tiltmeter data containing heat-induced noise (top graph) and filtered tiltmeter responses (bottom graph). Extreme regularity of the noise spikes allowed effective filtering of the data and a successful analysis of the downhole tilt data. ....	58
Figure 57. Log-log diagnostic plot.....	60
Figure 58. Square-root of time plot indicating no straight-line due to a varying derivative .....	61
Figure 59. Leakoff-normalized diagnostic plot.....	61
Figure 60. Tracer and Production Log: CGU 22-9 .....	62
Figure 61. Stress Test #1 and Stage 1 – Taylor .....	63
Figure 62. Stress Test #2 and #3.....	64
Figure 63. Stage #2 – Ardis and Roseberry Sands.....	65
Figure 64. Stage #3 – “E” and Justice Sand.....	66
Figure 65. Stress Test #4 – Davis Sand/Shale .....	67
Figure 66. Stage #4 – Bodcaw and Vaughn Sands .....	68

---

# 1. Summary

This report contains the results of Pinnacle Technologies' fracture engineering, well testing and downhole tiltmeter fracture mapping analysis of four hydraulic "waterfrac" treatments in the CGU 22-9 (Cotton Valley formation), located in Carthage, East Texas. The main purpose of this JIP Phase III (Joint Industry Project) was to characterize the geometry and growth of waterfracs (gel-less and low proppant concentration treatments) in the Cotton Valley formation. Microseismic fracture mapping of fractures in an offset well (CGU 21-10 JIP Phase I) initially indicated the possibility of asymmetric fracture growth, although more extensive processing later revealed a more symmetric shape. For this reason we performed downhole tiltmeter fracture mapping on the two upper treatment stages of the CGU 22-9 to determine if fractures grow asymmetrically or not. In order to accurately measure fracture length in *both* wings and thus address the question of lateral growth asymmetry, two tiltmeter arrays, consisting of nine tiltmeters each, were deployed in two offset producer wells (CGU 22-4 located 1378 ft. to the West and CGU 20-6 located 1341 ft. to the East of the treatment well). The location of these observation wells (Figure 1) are roughly in line with the anticipated fracture azimuth of N 70° E, previously obtained from microseismic imaging. Ideal placement of downhole tiltmeter arrays require they be lowered to a position where the tiltmeter in the middle of the array is at the same depth as the anticipated center of the fracture (often taken to be the middle of the perforated interval). This position maximizes the tiltmeter response to fracture-induced tilt changes thus increasing the accuracy in the measurement of fracture dimensions. Unfortunately, due to permanent packers at about 8,300 ft depth in both observation wells, we had to position the tiltmeter arrays significantly above the treatment intervals ranging from 8,645' to 9,614'. This prohibited mapping of Stages 1 and 2, but also rendered Stage 3 unmappable.

Stress testing (to determine shale and limestone stresses) was performed in four zones and well testing in two zones. The results of these tests were used to fine tune fracture modeling results and compare them with the microseismic imaging results in the CGU 21-10 and tiltmeter mapping results in the CGU 22-9.

## Main Objectives and Conclusions

We answered the following questions:

### 1. Are fractures asymmetrical?

Fracture growth in Stage 4 of the CGU 22-9 was asymmetrical. The ratio of asymmetry is about 2/3 to 1/3 with one wing growing about 1000 feet to the northeast (N 74° E) and the other wing about 600 feet to the southwest. (Figures 1 and 2) This result is similar to the original microseismic interpretation on the CGU 21-10. However, detailed post-processing of the microseismic results resulted in a more symmetric fracture. Unfortunately, the tiltmeter signals for Stage 3 could not be interpreted, in part due to the positioning of the arrays above permanent packers and high temperatures in the observation wells.

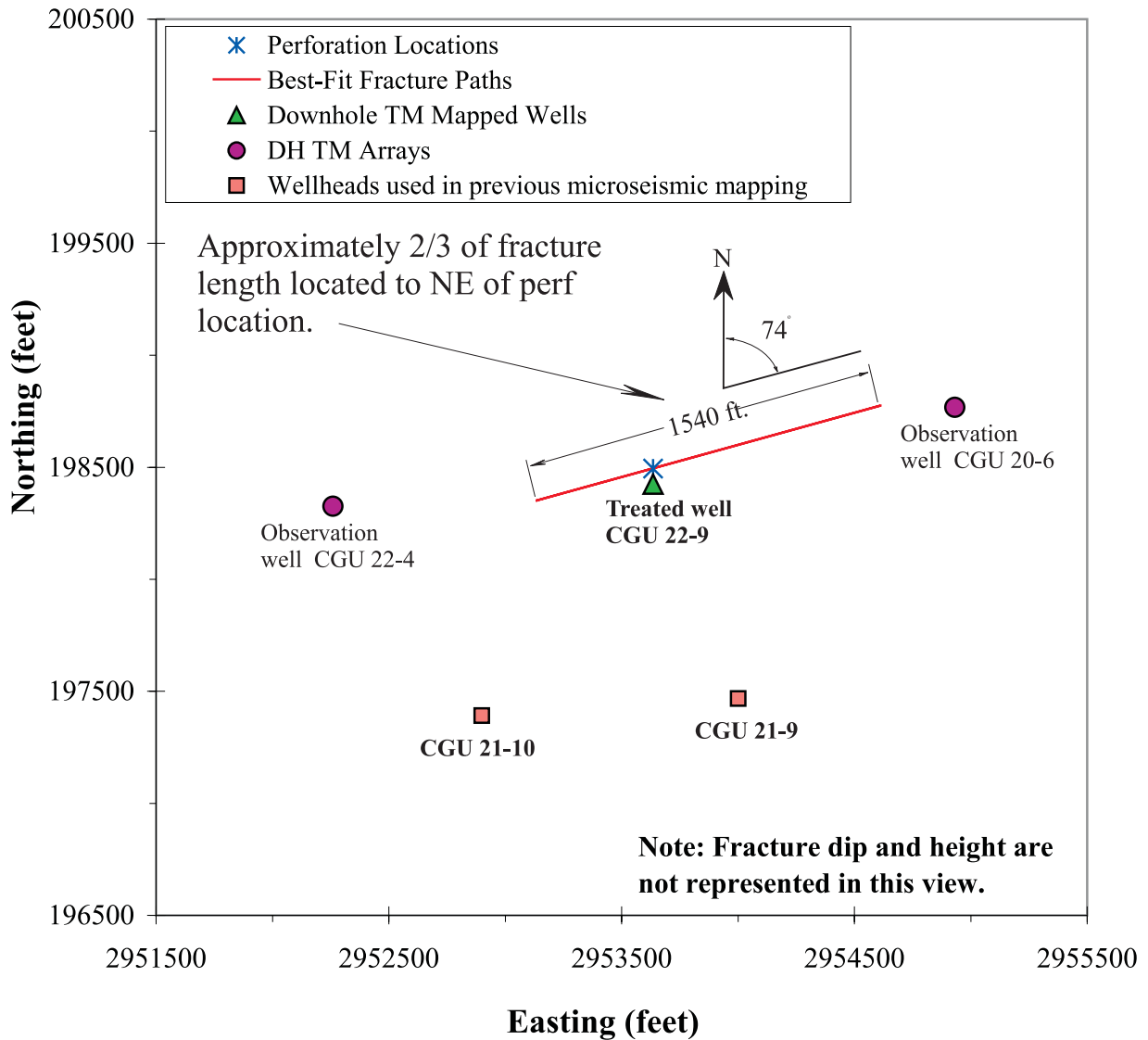


**Figure 1. Plan view of hydraulic fracture azimuth and length in Well CGU 22-9 illustrating positions of the treatment well and the two observation wells. Lateral asymmetry in the growth of the Stage 4 fracture is clearly evident with roughly 2/3 of the growth occurring to the NE towards observation well CGU 20-6 (red line).**

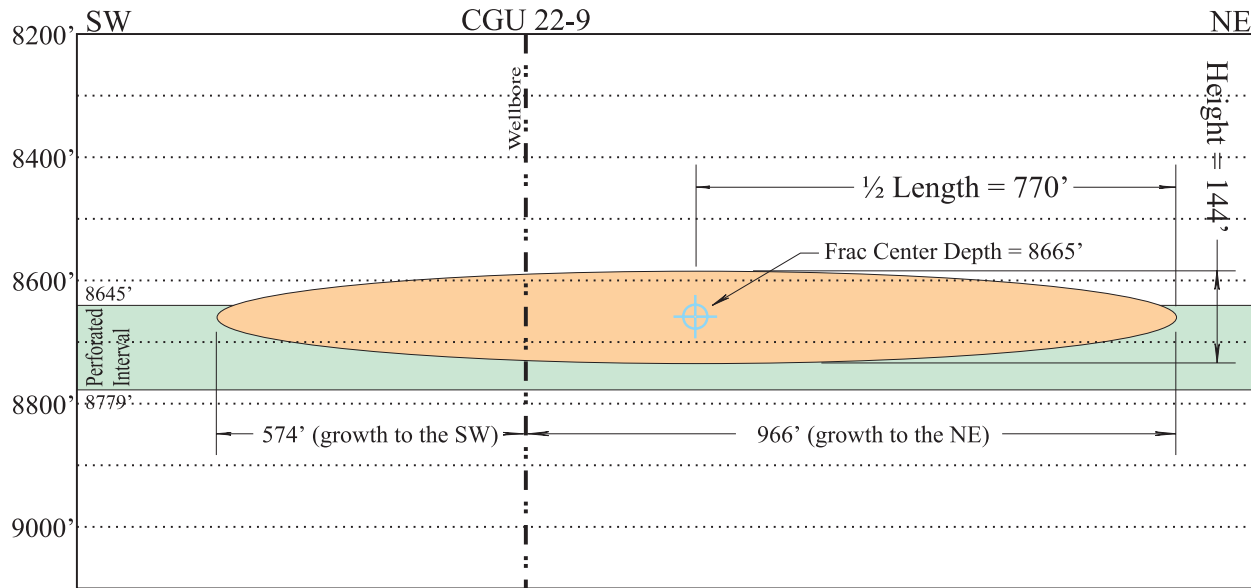


**Figure 2. Stage 4 fracture geometry from DH-tiltmeter mapping**

## 2. What is the hydraulic fracture geometry (height and length)?

Tiltmeter mapping showed a measured fracture half-length in Stage 4 of 770 ft with about 1,000 ft of the total length growing to the northeast of the well. The fracture height is about 150 ft (Figure 2). Due to the positioning of the array above the fractured interval, the fracture geometry measurements, while singular and unambiguous, do have a sizeable margin of error roughly equal to 30%. For this stage, fracture modeling resulted in 600 ft of half-length, which is within the “ballpark” of tilt mapping. However, fracture height (even with error margins) differs substantially with 460 ft of total fracture height growth in the model. In essence, tiltmeter mapping shows significantly more fracture containment than indicated by fracture modeling when using measured formation stresses. RA-tracers indicate fracture heights that are similar to the ones obtained from tiltmeter mapping, showing fracture containment. Below is a table that summarizes all geometry results from fracture modeling (Stages 1 through 4), tiltmeter mapping (Stage 4) and RA-tracers. Figure 3 shows the fracture geometries for all stages versus depth.

**Table 1 DH Tiltmeter , RA-Tracer and fracture modeling results for Well CGU 22-9**

Stage	Half-Length from DH-Tilt (ft)	Model Length (ft)	Height from DH-Tilt (ft)	RA-Tracer Height (ft)	Model Height (ft)
Stage 1 9,584'-9,614'	Not deployed	1,758	Not deployed	n.a.	159
Stage 2 9,150'-9,272'	Not deployed	983	Not deployed	205	323
Stage 3 8,935'-9,050'	n.a.	476	n.a.	215	442
Stage 4 8,645'-8,779'	770 (+175,-275) 495' – 945'	596	144 (+70,-30) 114' – 214'	200	464

Well CGU 22-9  
fractures vs. depth

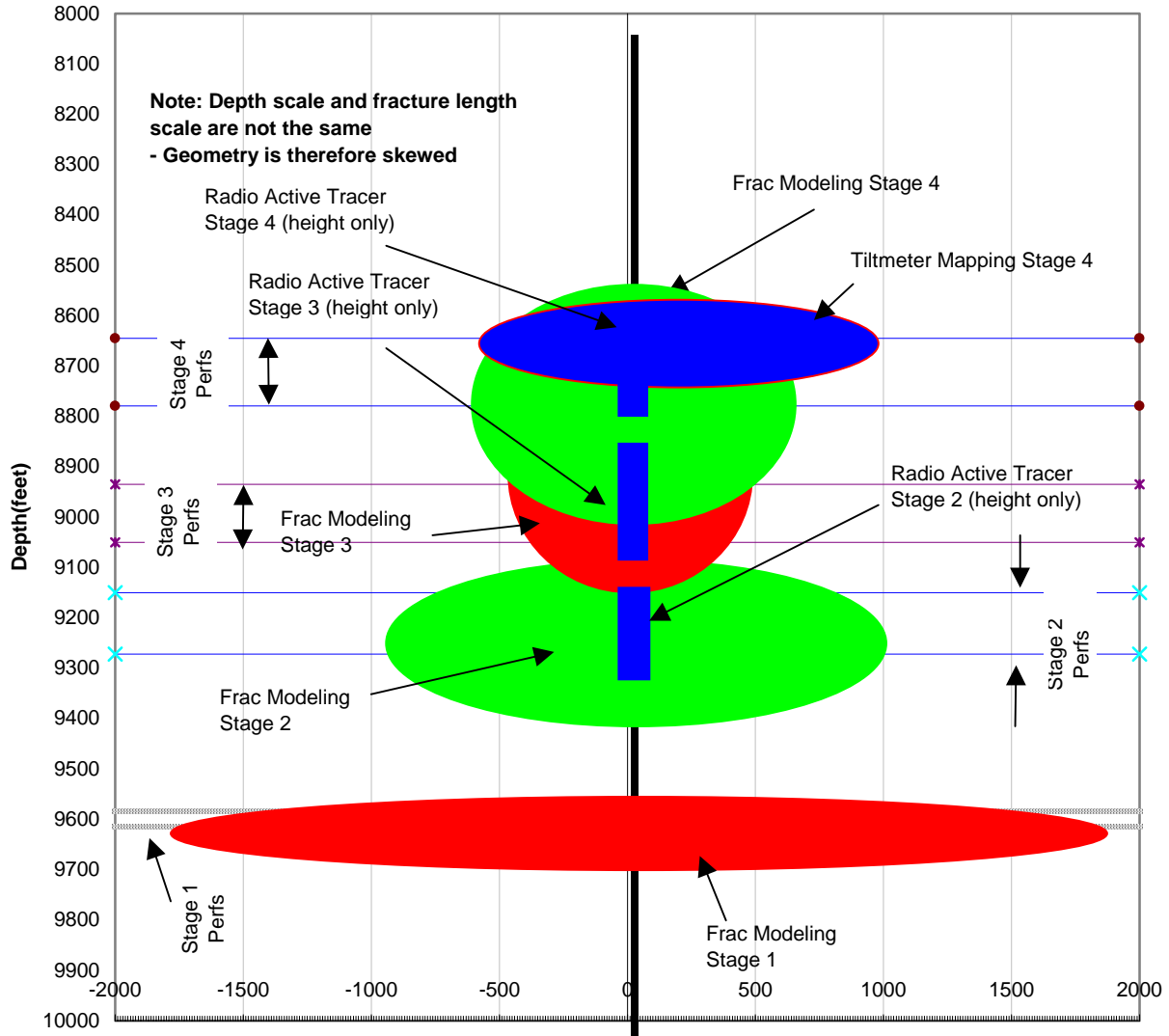


Figure 3. Fracture geometries from fracture modeling, downhole tiltmeter mapping and radioactive tracers for all 4 stages in the CGU 22-9

### 3. Stress Test and Well Test Results

A total of four stress tests were performed in selected intervals adjacent to pay zones. Closure stresses in the pay zones were determined from minifrac pressure decline analysis. Prefrac well tests were unsuccessful since it was not possible to establish any meaningful flow rates, possibly due to the complex wellbore configuration of two casing strings and large cement annuli. However, we successfully performed two postfrac PBU tests. The results of the stress tests are summarized in Figure 4 and well test results are listed in Table 2. The post-frac well test indicated substantial depletion in the Stage 1 Taylor zone (2,170 psi) and very short fractures. The 26 foot effective fracture half-length in the Taylor zone may be related to lack of proper cleanup due to extremely low reservoir pressure. The effective fracture length of Stage 2 was only 79 ft and is also substantially less than the fracture model length. Unfortunately, these well test results would indicate low quality fracture stimulation. However, we have also observed such short effective fracture lengths with standard x-linked propped fractures. These results would support the waterfrac hypothesis that inefficient cleanup of standard frac jobs may result in similar low quality fractures as waterfracs, however waterfracs are “cheaper”.

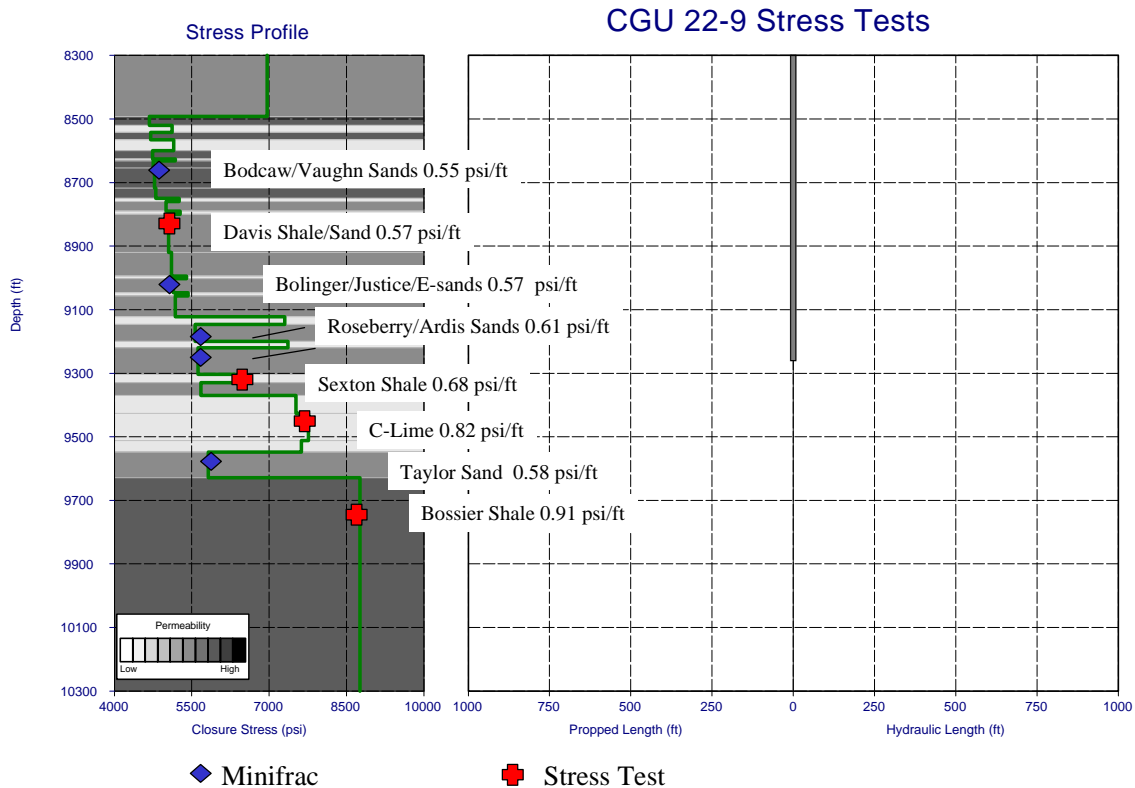


Figure 4. Stress profile with locations of stress tests and minifracs in the CGU 22-9

**Table 2. Well test results (CGU 22-9)**

Stage	Permeability/kh	Reservoir Pressure	Frac Half-Length	Conductivity/ Fracture skin	Post-frac flow
Stage 1 (Taylor)	0.02 md (postfrac) 0.63 md-ft	2,170 psi	26 ft	21 md-ft s=0.72	<100 MCFD @ 300 psi (surface)
Stage 2 (Roseberry/Ardis)	0.0057 md (postfrac) 0.68 md-ft	3,423 psi	79 ft	Infinite acting s=0	240 MCFD @ 280 psi (surface)

#### **4. What impact did stress measurements have on fracture modeling results? Are the results consistent with microseismic imaging and tiltmeter mapping results?**

Stress measurements imply that fracture growth based on 3-D frac models will be contained in the Taylor zone and fairly unconfined in the Upper Cotton Valley. However, both microseismic fracture mapping and tiltmeter mapping indicated some fracture confinement in the Upper Cotton Valley. Microseismic imaging indicated that Stage 2 in the CGU 21-10 seemed to be confined by the Davis sand/shale interval. However, stress tests in the CGU 22-9 revealed a stress gradient of only 0.57 psi/ft in this section, which is by no means enough to confine height growth from stress effects alone. Other mechanisms besides stress must be causing confinement. The Davis section consists of highly laminated shale/sand sequences. Recently it was postulated, based on actual tiltmeter measurements, that a “composite material (layer) effect” (similar to composite materials that arrest crack growth) could inhibit fracture height growth. Tiltmeter mapping of Stage 4 in the CGU 22-9 also showed substantially more height confinement than predicted by the 3-D fracture model. Unfortunately, these conclusions imply that even with rigorous stress test measurements, it may not be possible to properly model fracture height growth unless other diagnostic measurements of fracture height are utilized.

#### **5. Production Log Results**

The production log showed most of the production (50%) coming from the uppermost stage (Stage 4 Bodcaw/Vaughn sands). The Taylor (Stage 1) and Roseberry/Ardis zones (Stage 2) only contribute 14% each and the Bolinger/Justice/E-sand (Stage 3) zone about 23%. The total flow rate at the time of the production log was about 1,140 MCFD.

## 2. Downhole Tiltmeter Analysis

Two downhole tiltmeter arrays (each consisting of nine individual tiltmeters) were deployed within adjacent observation wells CGU 22-4 and CGU 20-6 located at horizontal distances of approximately 1400' and 1325' from the perforated intervals of well CGU 22-9. Downhole tiltmeter fracture mapping was performed on the third and fourth stage treatments to characterize fracture growth including depth to fracture center, height, half-length, and perhaps **most importantly, lateral fracture asymmetry**. For this reason we selected observation wells on both sides of the treatment well, roughly in the direction of the expected fracture azimuth (Figure 5). Such a configuration allows for maximum sensitivity of the tiltmeter signals to fracture length on both sides of the treatment well (symmetry of fracture) due to the fact that tilt magnitudes change with the distance cubed between the fracture and the tiltmeter array. (Figure 6) (i.e. if the fracture position is 50% closer to the array, tilt magnitudes change by a factor of 8). Despite plans to map both Stage 3 and 4 fractures, success was only attained with the Stage 4 treatment. The presence of permanent packers prevented placement of the tiltmeter arrays at a depth equal to the perforated interval and required that tilt measurements be taken from 990' and 1060' above the fractured intervals. This placement, coupled with difficulties associated with the 240°F temperatures encountered at depth, prevented the acquisition of useable data for Stage 3 and rendered it unmappable. The shallower perforated interval of Stage 4 (280' higher) and modified data collection techniques for the high temperatures enabled successful mapping of the Stage 4 fracture detailed in this report. Table 3 and Figures 5 and 7 show the results of the downhole tiltmeter analysis for Stage 4. The results will be discussed in Sections 2.1 and 2.2.

**Appendix A** gives a brief overview of how downhole tiltmeter fracture mapping works and how fracture geometry is inferred from the measured tiltmeter signals. **Appendix B** discusses issues of temperature sensitivity encountered with the downhole tiltmeter array.

**Table 3. Downhole tiltmeter fracture mapping results for Stage 4 CGU 22-9 listing fracture size, depth, and laterally asymmetric growth to the NE along with error bounds.**

Well	Treatment Date	Perforated Interval (ft.)	Vertical Extent (ft.)	Fracture Height (ft.)	Fracture Half-Length (ft.)
CGU 22-9	04/22/99	8645-8779	8593-8737	144 (+70, -30)	770 (+175, -275)

Well	Treatment Date	Fracture center shift to the NE along the fracture azimuth (ft.)	Lateral Asymmetric Growth
CGU 22-9	04/22/99	196 ± 65	60% to the NE

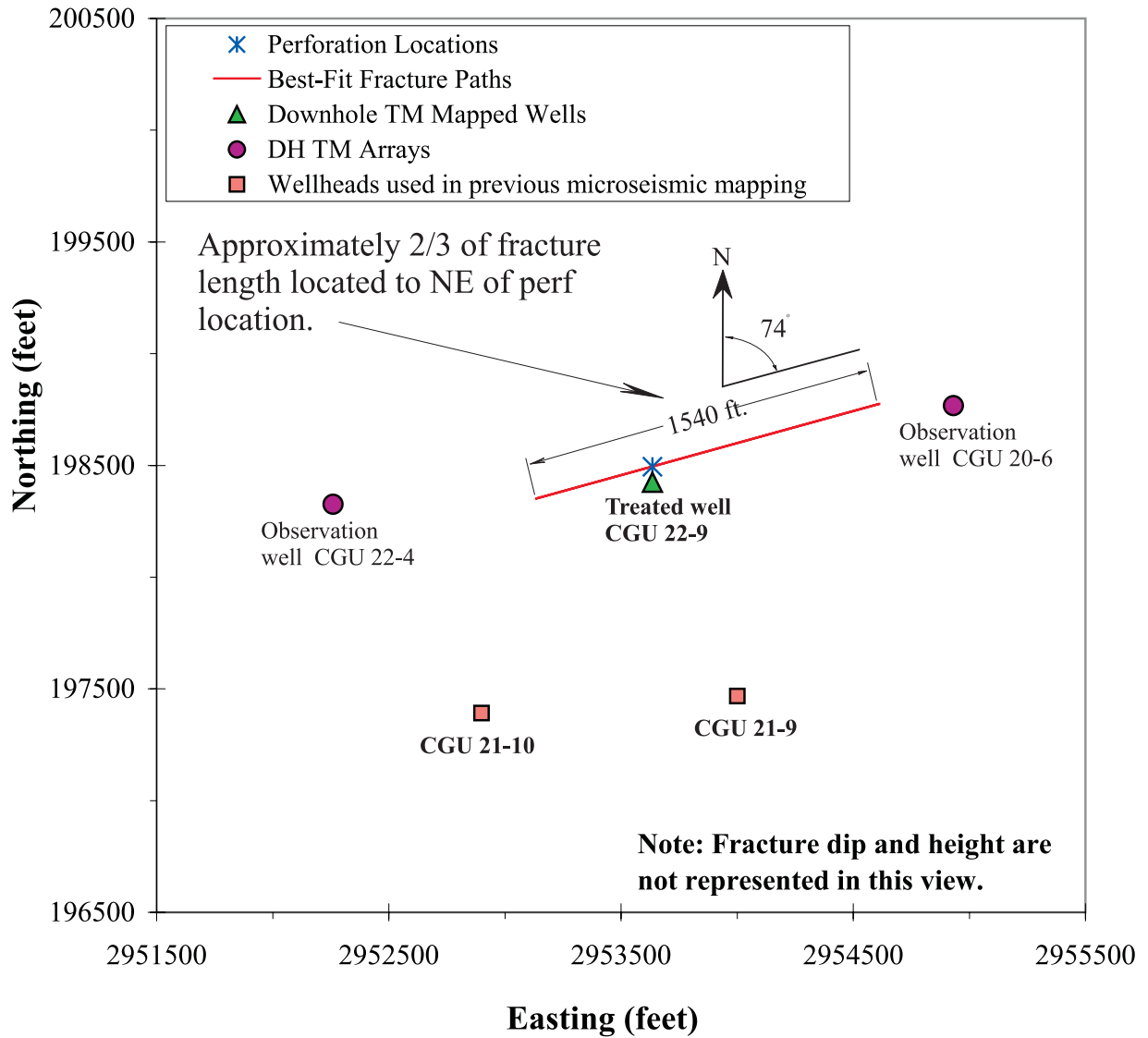


Figure 5. Map view of treated well CGU 22-9, observation wells CGU 22-4 and CGU 20-6, and the fracture half-length and azimuth for Stage 4 downhole tiltmeter fracture mapping results.

## DOWNHOLE TILT MAPPING OF FRACTURE LENGTH

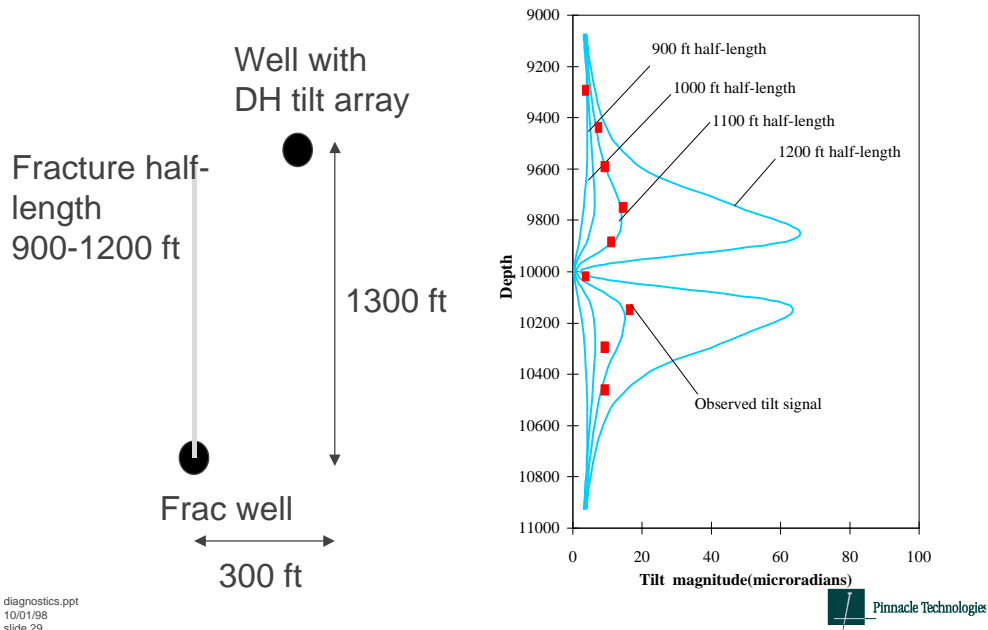


Figure 6. Sensitivity of tilt magnitude as fracture grows towards an observation well

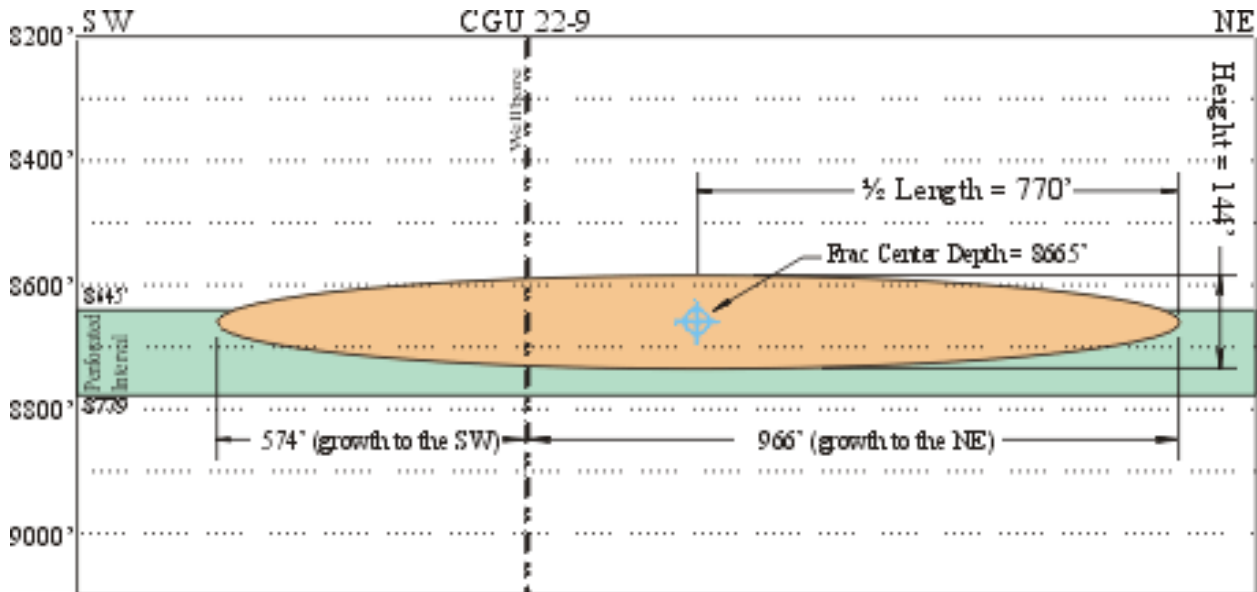
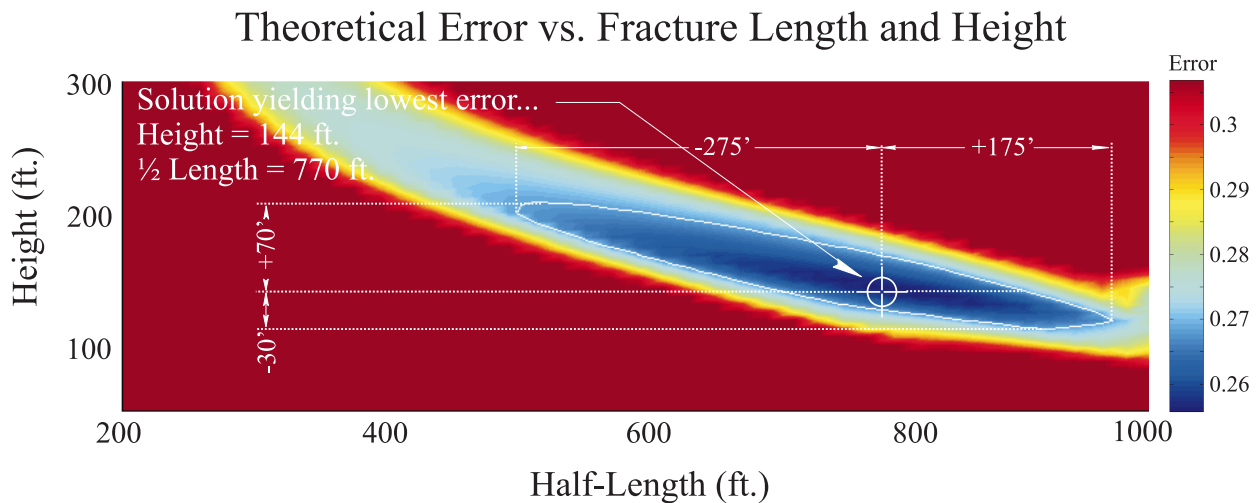


Figure 7. Fracture profile for Stage 4 in the CGU 22-9 well illustrating fracture size, target zone coverage, and significant lateral growth asymmetry.

## 2.1 Discussion of Error Bounds

Error bounds for downhole tiltmeter fracture mapping are obtained by calculating a contour which defines the limits of mapping resolution (Figures 8 and 11). Figure 8 illustrates the process by which the solution, and its associated error, is determined for fracture height and half-length. A two dimensional space is defined by assigning a range of possible height and half-length values to the X- and Y-axes. An “error” is computed by comparing theoretical tilt values generated with a specific combination of height and half-length with the actual tilt responses measured by the tiltmeter arrays. Parameter combinations yielding the lowest error provide a range of possible solutions. Combinations yielding an error equal to the resolution limits of the downhole fracture mapping technique define a contour surrounding the solution point. Analyses with ideal data show a steep error gradient close to the solution point, thus the error boundary contour defines a small “parameter space”. When noise, insufficient data, or data from complicated geometries is introduced into the analysis process the gradient lessens and the error boundary grows to include more combinations of height, half-length, or whatever fracture parameters are being evaluated. In this way fracture offset was also evaluated to characterize lateral asymmetry (Figure 11).



**Figure 8. Theoretical error as a function of fracture height and half-length values. Crosshairs mark parameter values producing best match between actual and theoretical tiltmeter responses. White contour defines the resolution limit boundary around the solution point.**

## 2.2 Lateral Fracture Growth Asymmetry

Larger tilt responses from the downhole tiltmeter array located within observation well CGU 20-6 (NE of the treatment well) strongly indicate significant lateral asymmetry in the growth of the Stage 4 fracture in the CGU 22-9 (Figure 5). The average tilt magnitude in the CGU 20-6 is about 2-times larger than in the CGU 22-4 (Figure 9). Minor differences in the distance of each well to the treatment well and relative orientation of the fracture azimuth between the two observation wells do not account for the sizeable difference in tilt magnitude between the two arrays (distances differ by only about 75'). Only asymmetrical growth of the NE fracture wing towards the CGU 20-6 array realistically accounts for the discrepancy. A fracture center offset of approximately 200' is adequate to produce the larger signals seen in the NE array. Figures 9 and 10 illustrate the fit of theoretical and actual tilt responses from downhole tiltmeter arrays in the two observation wells. The error maps in Figs. 8 and 11 are a result of this fitting process. Due to the arrays being well above the actual perforated intervals, it is obvious why fracture geometry estimates (Table 3) have fairly large errors associated with them. The characteristic "hump pattern" of the tilt signals is below the array across from the treatment interval. However, the slope or trend of the data leading to the hump pattern gives a clear indication of the tilt magnitudes, showing fracture asymmetry, and confine the geometry solution to certain bounds of height and length. Figure 9 shows the best fit for a fracture center offset approximately 200' to the NE due to asymmetric growth in that direction. Figure 10 illustrates the best fit for a fracture with lateral symmetry (centered at the perforated interval of the treated well). Differences between tilt responses from the shifted and unshifted fractures are significant for both arrays. At observation well CGU 22-4 theoretical tilt responses from an offset fracture very closely match the actual trend of the real data, as opposed to the symmetrical fracture in Fig. 10. The match at CGU 20-6 also greatly improves when the fracture is offset. Theoretical tilt values for the lower portion of the array rise significantly to more closely match the actual instrument responses and the curve more closely fits the ideal response

Analysis error vs. asymmetrical lateral fracture growth (modeled as a lateral offset in the fracture center) is illustrated in Figure 11. Here, error is computed through the comparison of measured tiltmeter responses to theoretical tilt responses generated by a hypothetical fracture of a given size, shape, and orientation. Lower error values correspond to those fractures, which would generate tilt responses most like those actually recorded by the instruments. In Figure 11 a hypothetical fracture is evaluated at numerous positions along the presumed N 74° E azimuth. The lowest error is located about 196' to the Northeast. This solution, while singular and unambiguous, does have a sizeable margin of error roughly equal to 8% of fracture half-length. This error may be attributed to the low signal-to-noise ratio introduced by the high temperatures and the unfavorable depths of the two arrays in relation to the fracture center.

2. Downhole Tiltmeter Analysis

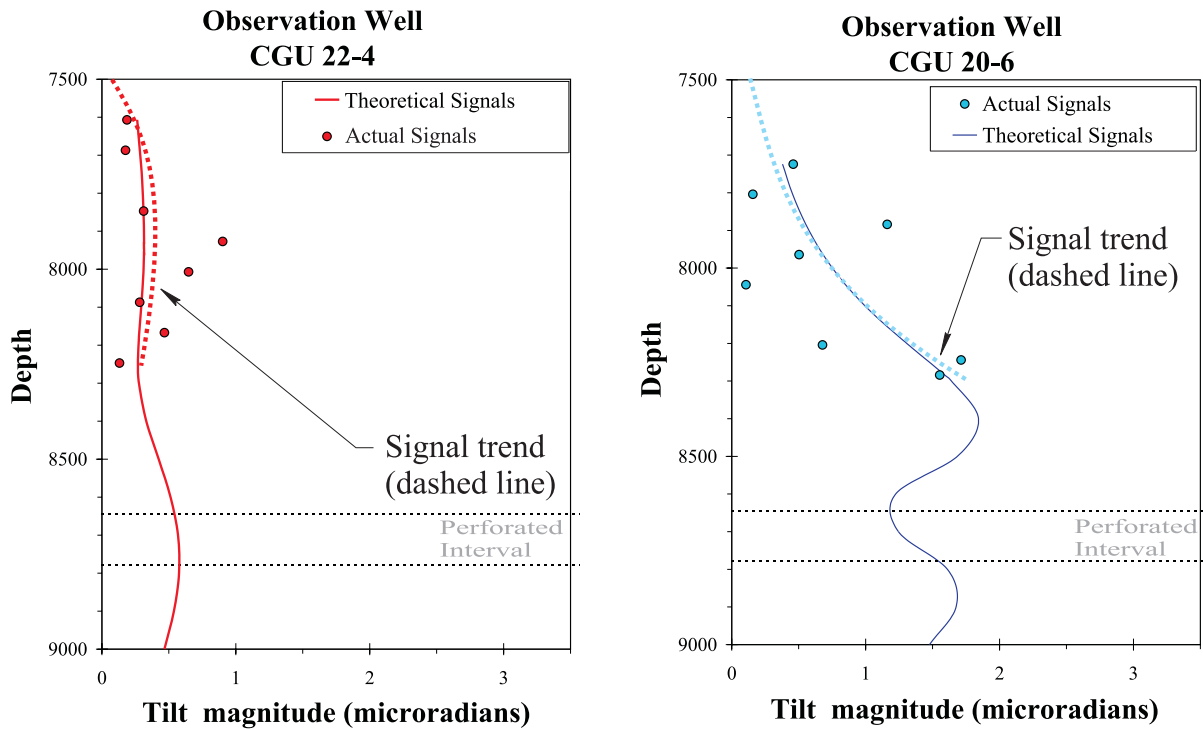
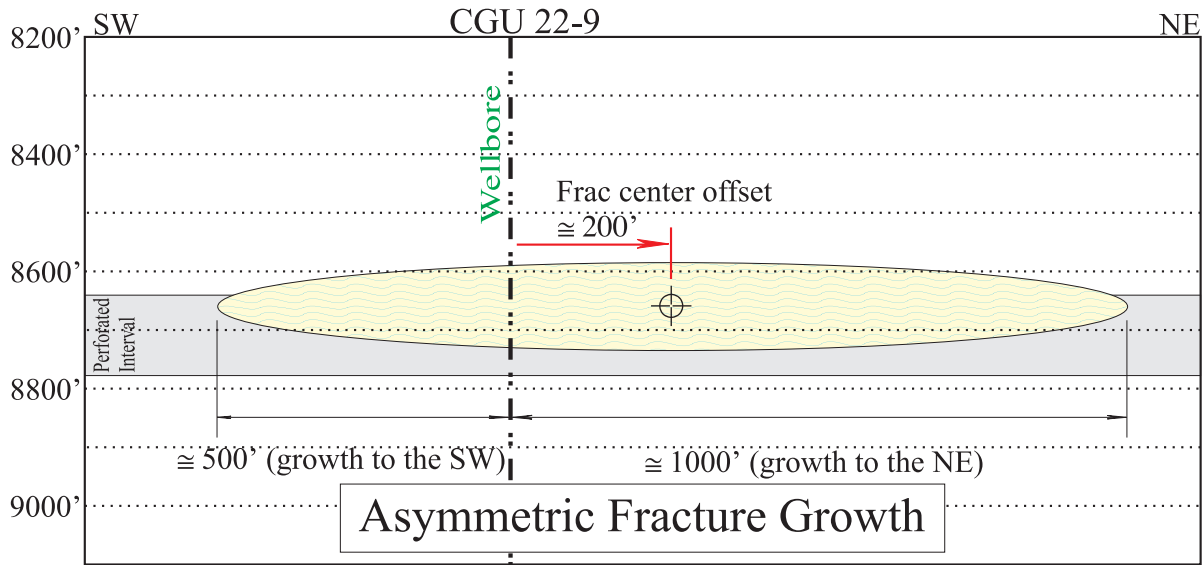


**Figure 9. Theoretical, actual, and ideal tilt responses for each tiltmeter array in Stage 4 of well CGU 22-9 when allowing for asymmetric fracture growth. Note closer agreement between theoretical and ideal tilt responses in observation well CGU 20-6 when fracture is shifted approximately 200' to the NE as shown here.**

2. Downhole Tiltmeter Analysis

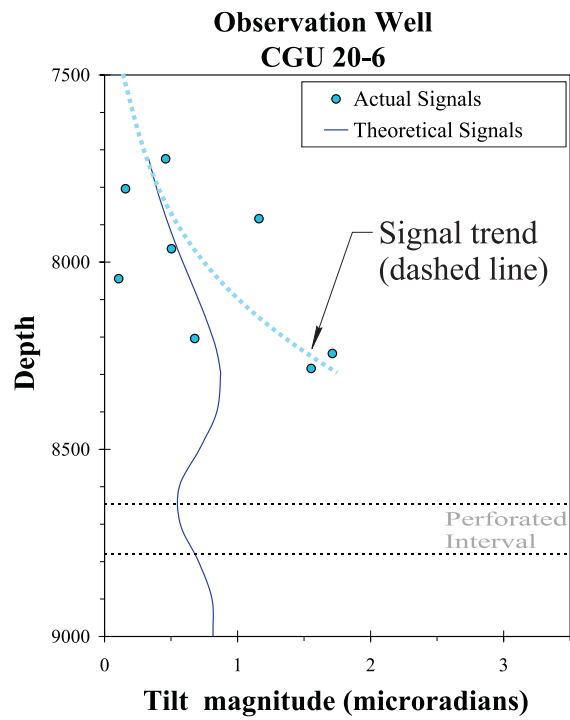
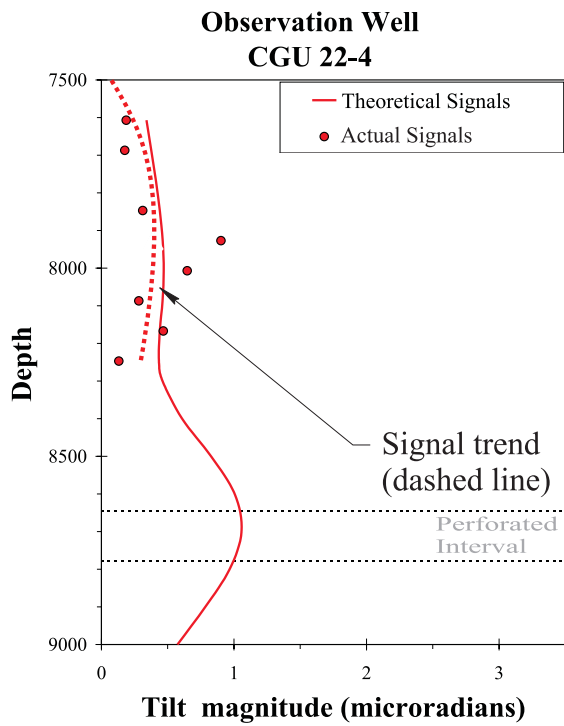
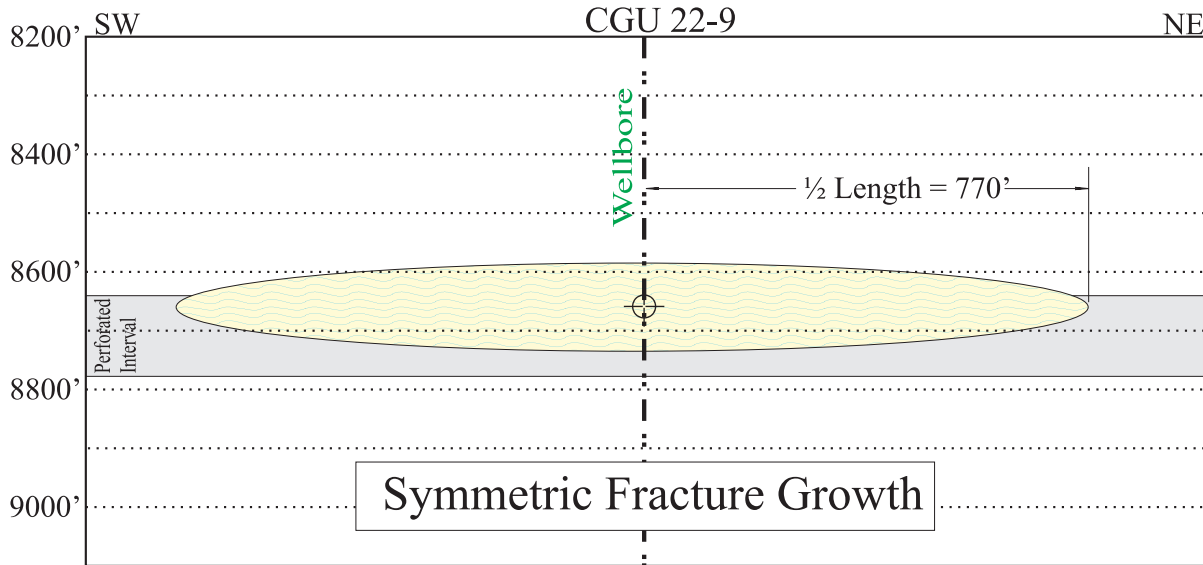


**Figure 10. Theoretical, actual, and ideal tilt responses for each tiltmeter array in Stage 4 of well CGU 22-9 when assuming symmetric fracture growth. Note larger tilt responses for instruments within the array located at observation well CGU 20-6. A fracture with lateral symmetry would produce tilt magnitudes that are smaller than the measured ones in the CGU 20-6.**

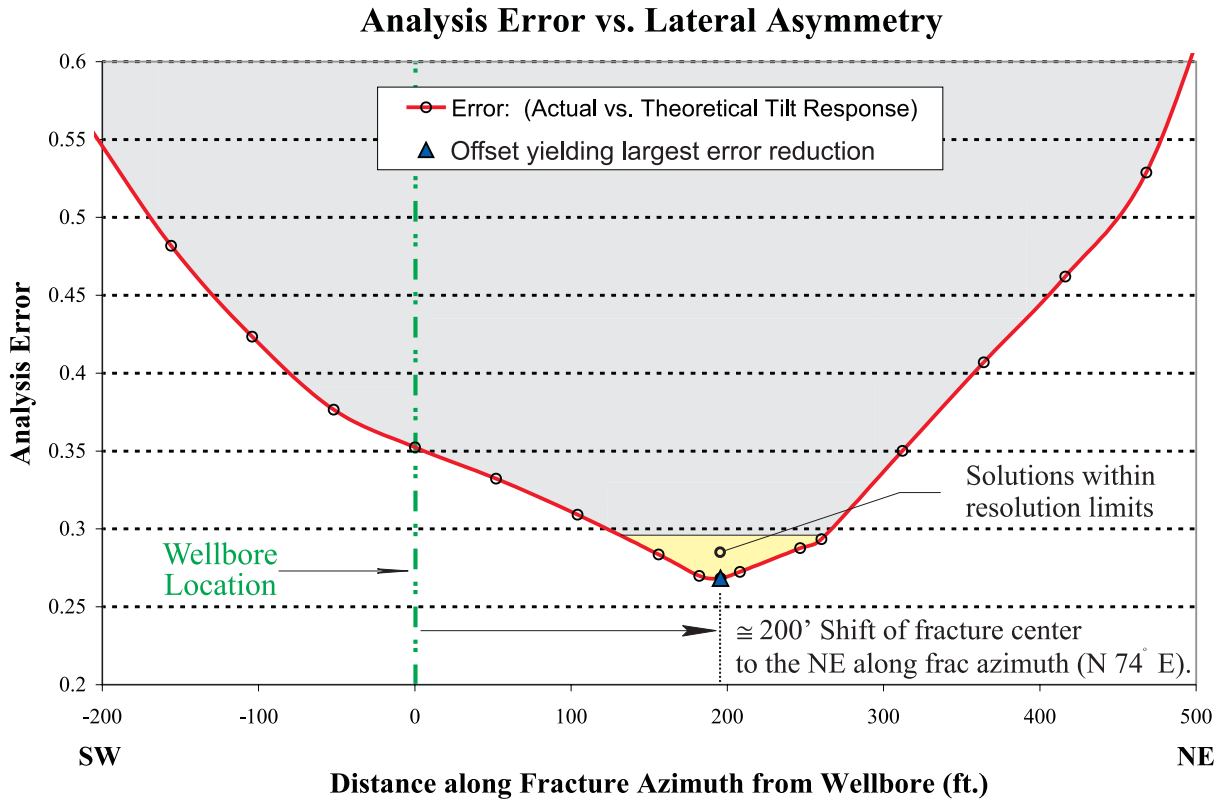


**Figure 11. Error plot illustrating fracture lateral asymmetry. Fracture center (blue triangle at bottom of curve) has shifted approximately 200 feet along the fracture azimuth away from the wellbore to the NE. Yellow region at bottom of curve defines the resolution limits of the analysis.**

### 3. Stress Testing

This section outlines the results from four stress tests in the CGU 22-9, which were performed to quantify stress gradients in shales and limestones within the Cotton Valley. The stress tests induced small fractures by pumping small volumes of KCL-water (1 to 8 bbls at 1-2 bpm) into two foot intervals, perforated with 60 degree phasing and four shots per foot. Closure was estimated by analyzing the pressure falloff after each injection. Injections were repeated for each test and injected volume was increased for subsequent injections. Table 4 summarizes the tested intervals and results, and Figure 12 shows the entire stress profile including pay intervals:

**Table 4. Results of stress tests**

Stress Test	Stress Gradient (psi/ft)
Test 1 (Bossier Shale)  9,688'-9,690'	0.91
Test 2 (C-Lime)  9,458'-9,460'	0.82
Test 3 (Sexton Shale)  9,318'-9,320'	0.68
Test 4 (Davis Shale/Sand)  8,862'-8,864'	0.57

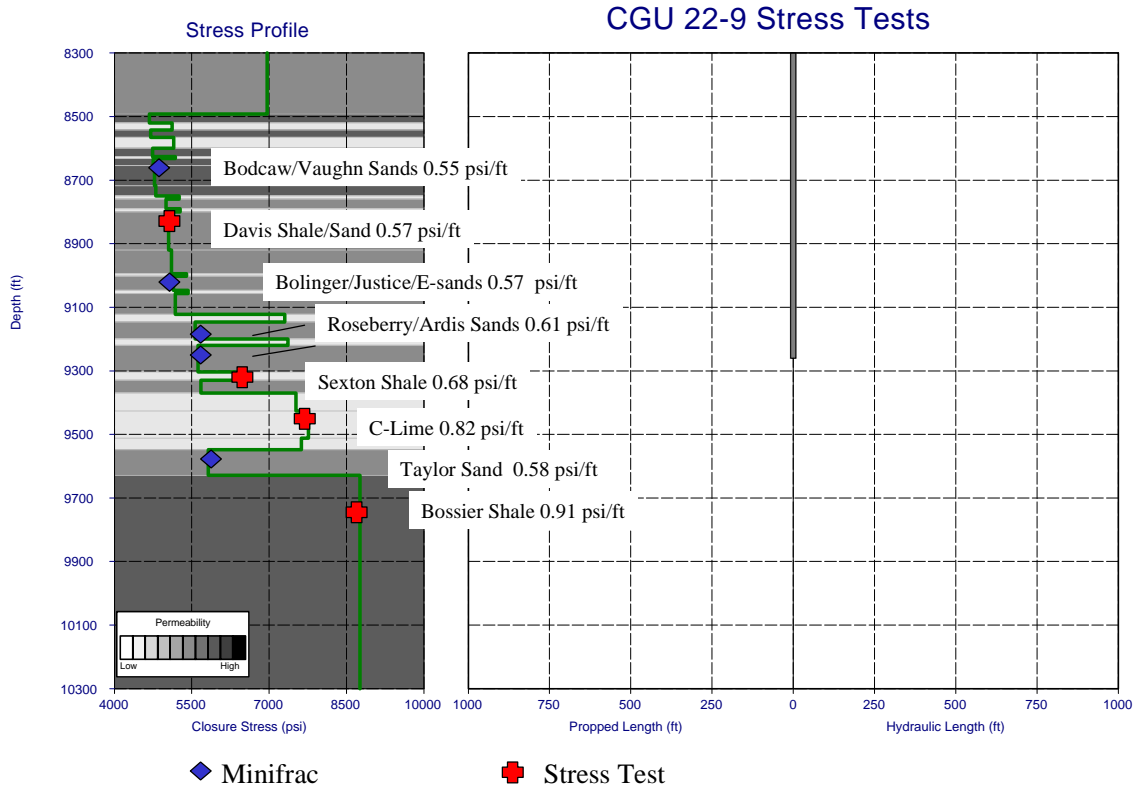


**Figure 12. Measured stress profile in the CGU 22-9**

The following section includes the data and analysis for each stress test. The CGU 22-9 was one of the microseismic observation wells used in Phase I of this project. The unusual wellbore configuration of 2-7/8" casing with a strapped-on geophone array cemented inside 7-5/8" casing, which in turn is cemented inside 9-7/8" hole complicated the analysis of most of the tests (Figure 13). The perforation effectiveness through two sets of pipe with two cement sheaths is very questionable, especially since it was only possible to use 2-1/8" RTG, 6.7 gram charged HSC guns instead of expendable guns. We observed unusually large pressure drops during the injection falloffs and rapid leakoff in most of the cases (we expected very slow declines due to extremely low shale permeability). Such a response together with fracture gradients of more than 1.05 psi/ft may be a result of a very complex near-wellbore fracture geometry (many multiple cracks propagating in several directions). We used several pressure decline analysis techniques such as square-root of time plots and, more importantly pressure transient diagnostic techniques (log-log plots). Despite the complexity, we believe to have obtained fairly reasonable stress values. The first stress test in the Bossier shale is described in more detail to demonstrate the general analysis procedures.

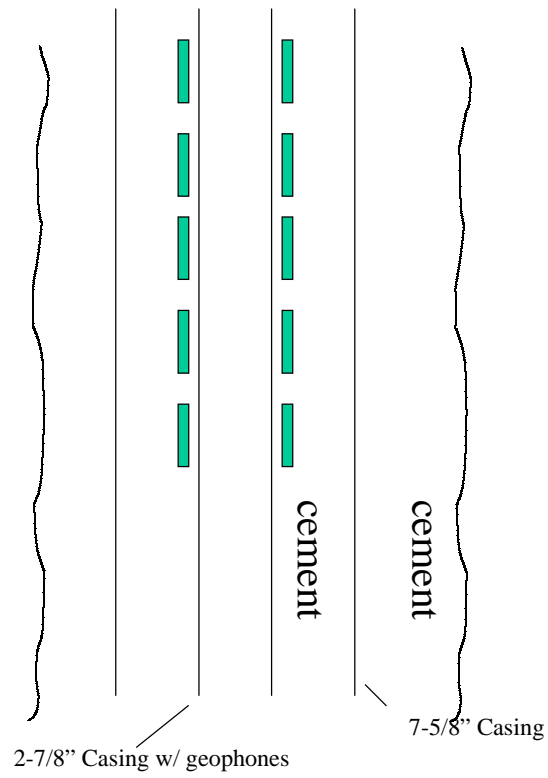


**Figure 13. Wellbore configuration: CGU 22-9**

### 3.1 Stress Test Results and Analysis

We analyzed the pressure decline data using log-log diagnostic plots (as used in standard pressure transient analysis) both of the pressure and leakoff-normalized pressure to identify closure pressure (*Mayerhofer et al.:" Pressure Transient Analysis of Fracture Calibration Tests," JPT March 1995*). **Appendix C** describes the methodology of using log-log diagnostic plots. For some injections we also used the flow pulse technique (*Wright et al.:"Robust Technique for Real-Time Closure Stress Determination", SPE 30503*) as an alternative technique to determine closure pressure and the standard square-root of time analysis technique.

#### 3.1.1 Stress Test #1 – Bossier Shale (9,688’-9,690’)

Stress tests were pumped with KCl-water in six injection cycles starting with small volumes at first and then increasing to larger volumes. After loading the hole with 0.8 bbls of water, pressure started increasing and quickly rose to maximum surface pressure, which was set at 6,300 psi - 6,500 psi. Table 5 is a summary of the injection data and closure estimates.

**Table 5. Stress Test #1 results**

Injection	Surface Pressure	Volume	Average Rate	Closure
#1	6380 psi	2.0 bbls	0.6 bpm	-
#2	6110 psi	1.8 bbls	1.0 bpm	-
#3	6308 psi	3.0 bbls	0.6 bpm	0.90 psi/ft
#4	6421 psi	4.0 bbls	0.5 bpm	-
#5	6500 psi	3.0 bbls	0.25 bpm	-
#6	6600 psi	7.0 bbls	0.35 bpm	0.91 psi/ft

CGU 22-9 Stress Test #1  
 Bossier Shale 9,688'-9,690'

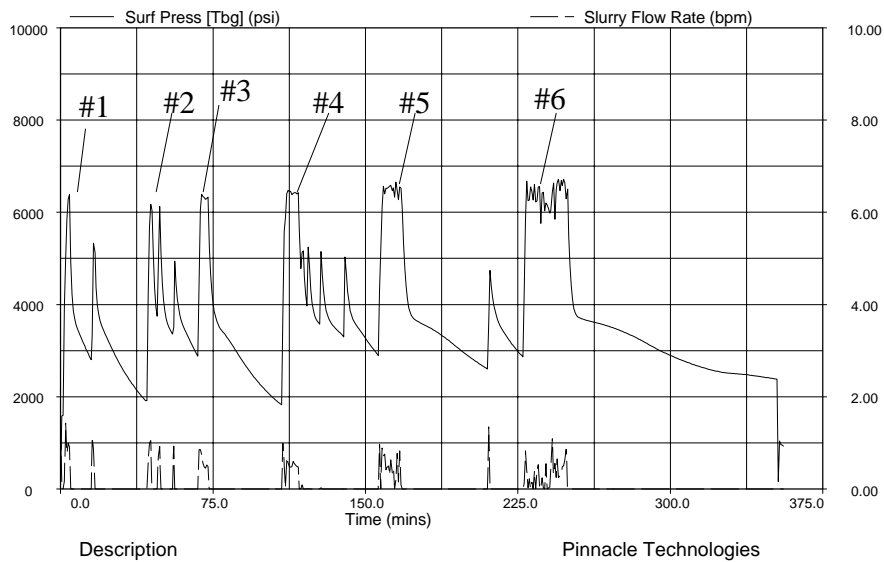


**Figure 14. Stress Test #1 injection history**

Figure 14 shows the entire injection history. Since pressure increased after only 0.8 bbls as the hole was loaded and the fluid level would have required 7.8 bbls to achieve a full column of water, gas was entrapped in the loading process. Injection pressures increased slightly for every injection. In the later injections the pump could not sustain a stabilized injection rate at maximum pressure. To avoid this problem a pump with smaller plungers was used on subsequent stress tests.

***Injection #1***

Pressure quickly reached the maximum surface pressure of 6,300 psi. No clear breakdown or “flattening out” of the pressure was detectable. It seems unlikely that a single planar fracture was created. Bottomhole treating pressure was about 1.1 psi/ft (wellbore friction was negligible), which is about equal to the overburden stress. After shutdown, pressure declined rapidly by about 2,400 psi within 2 to 3 minutes. A pressure pulse was pumped after 11 minutes of falloff at about 2,800 psi to verify if a fracture was open or closed. As expected it showed no open fracture at this pressure (pressure remains at higher ISIP and declines parallel to previous decline - Figure 15). Log-log diagnostic plots both of the pressure and leakoff-normalized pressure are shown in Figures 16 and 17. The plots reveal no clear linear flow regime but some complex reservoir flow is present as indicated by the hump in the data (possibly multiple cracks forming a complex pattern of fluid leakoff). Perforating through two strings of casing with two cement sheaths may have created a complex system of small cracks in all directions, making it difficult to clearly identify linear flow from a planar fracture and the minimum horizontal stress.

CGU 22-9 Stress Test #1  
 Bossier Shale 9,688'-9,690'

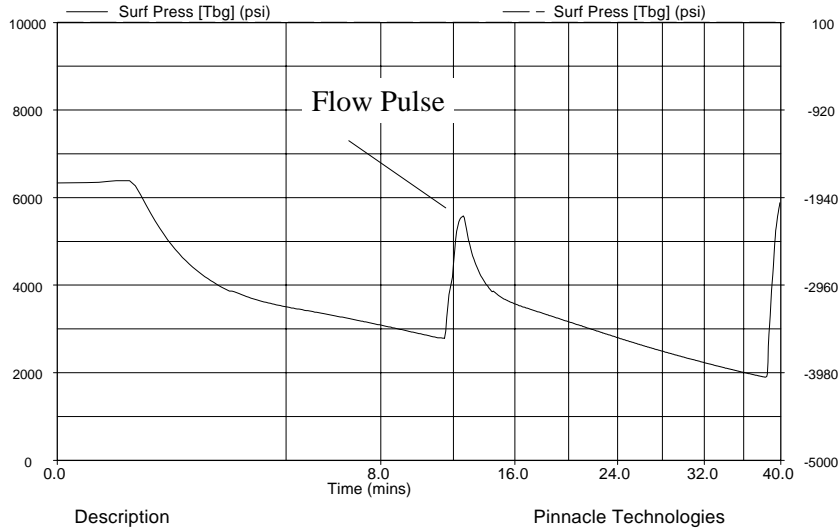


Figure 15. Injection #1: Pressure falloff with flow pulse shows closed fracture

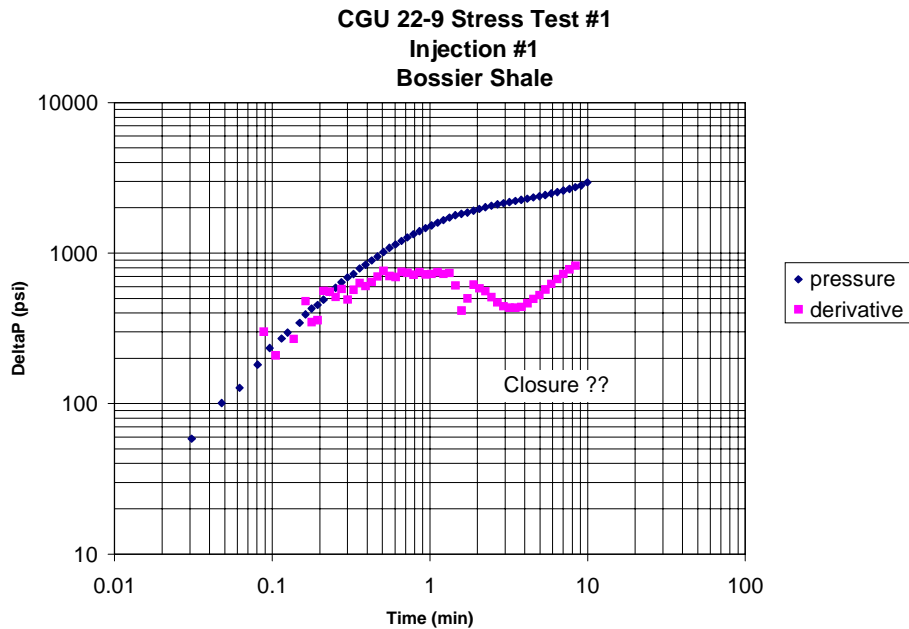
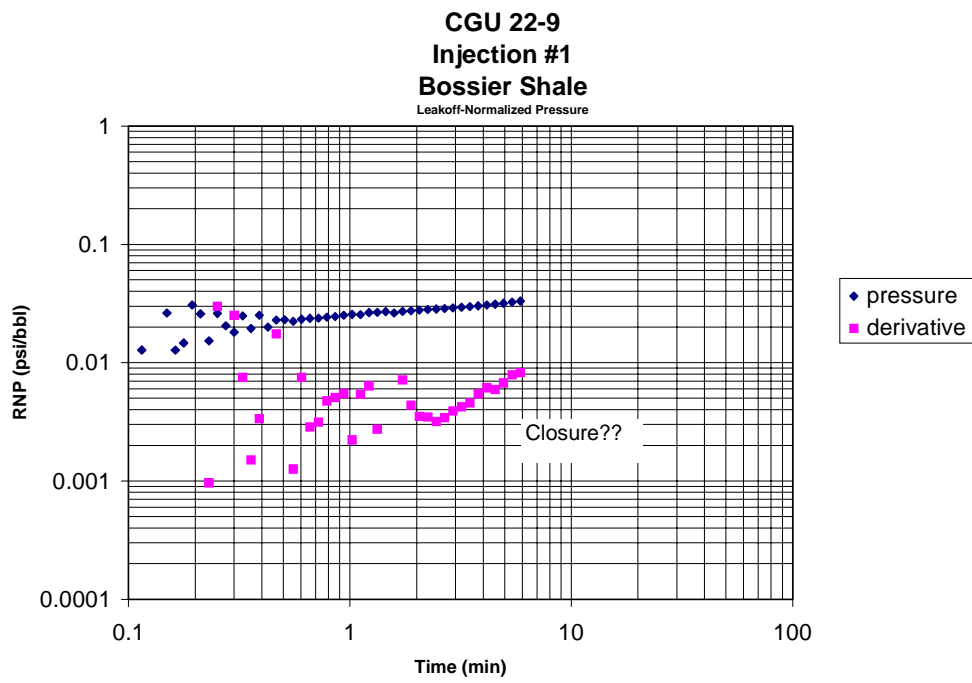


Figure 16. Injection #1: Log-log diagnostic plot of pressure decline



**Figure 17. Injection #1: Leakoff-normalized diagnostic plot**

**Injection #2**

This injection behaved like the first one. Injection pulses showed a closed fracture at all times (Figure 18).

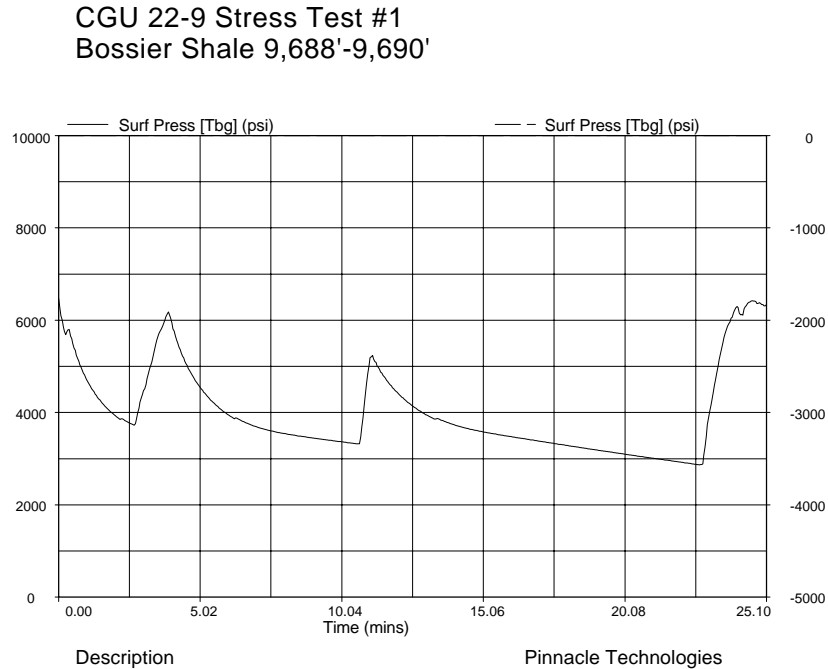


**Figure 18. Injection #2: Pressure falloff with flow pulses shows closed fracture**

**Injection #3**

During this test, pressure “flattened out” at about 6,300 psi while injecting at a constant 0.5 bpm rate. This seemed to indicate a stable fracturing process. No flow pulses were conducted during this falloff. Log-log diagnostic plots both of the pressure and leakoff-normalized pressure are shown in Figures 19 and 20. The leakoff-normalized pressure (Fig. 20) reveals linear flow up to about 1.8 minutes of falloff and then departs into the hump as already observed in the previous injections. We picked closure at the point of departure, which corresponds to a surface pressure of about 4,480 psi (8,690 psi BHP) or 0.90 psi/ft closure stress gradient. Similar to the first injection some complex reservoir flow is present in later time. In this case there is an indication of 1/4-slope to 1/3-slope behavior in late time indicating the possibility of some residual crack pattern.

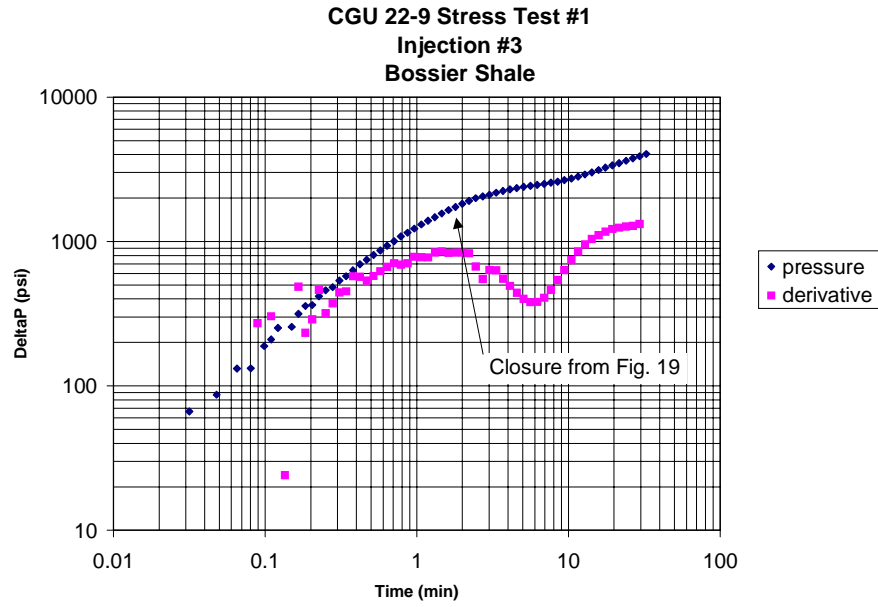


**Figure 19. Injection #3: Log-log diagnostic plot of pressure decline**

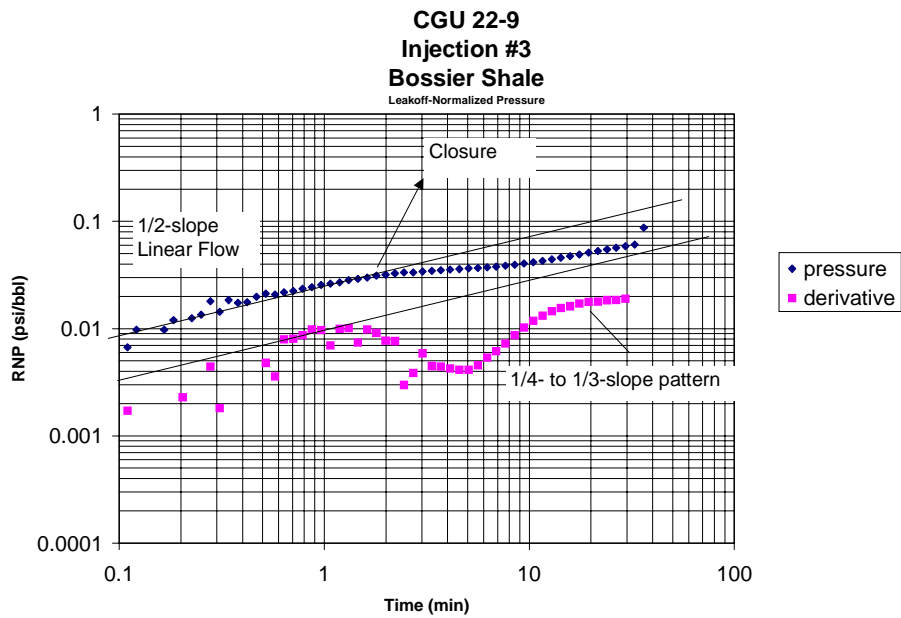


**Figure 20. Injection #3: Leakoff-normalized diagnostic plot**

**Injection #4**

This injection included flow pulses in early time starting at about 4,600 psi surface pressure. Figure 21 shows the flow pulses, which indicate no open fracture for the entire falloff (pressure remains at higher values for several minutes and declines parallel to previous decline). This means, that the closure pressure determined in Injection #3 could not be verified by this injection.

**CGU 22-9 Stress Test #1  
 Bossier Shale 9,688'-9,690'**

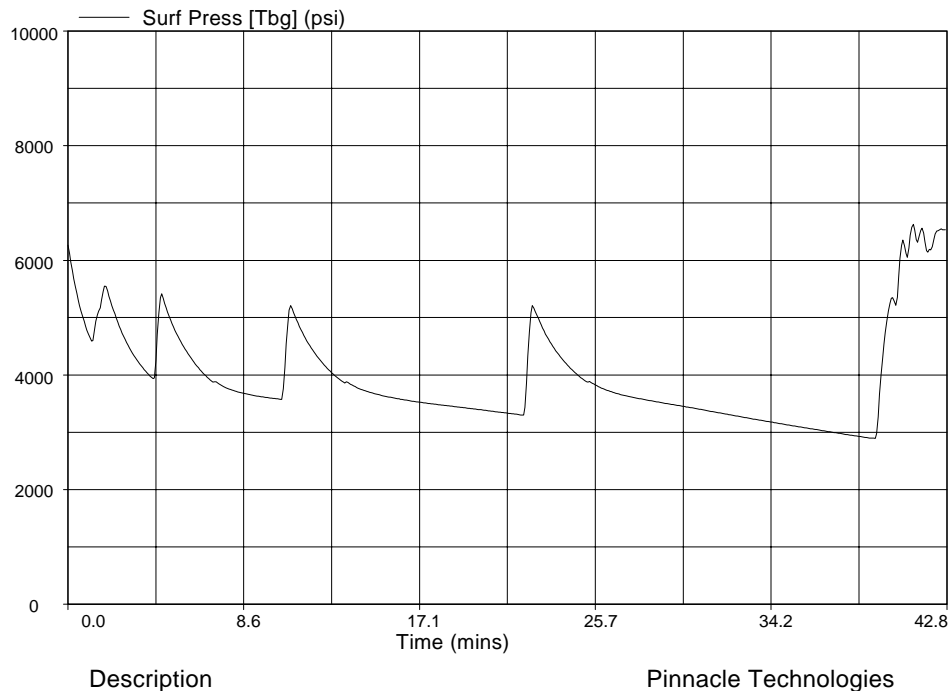


**Figure 21. Injection #4: Pressure falloff with flow pulses shows closed fracture**

**Injection #5**

The high-pressure pump had problems sustaining a stable injection rate at maximum pressure. Log-log diagnostics (Figures 22 and 23) show that the linear flow detected in Injection #3 is not present. Again complex reservoir flow is present as indicated by the hump in the data and late-time 1/4-slope to 1/3-slope behavior. Closure pressure cannot be determined from this pressure falloff.

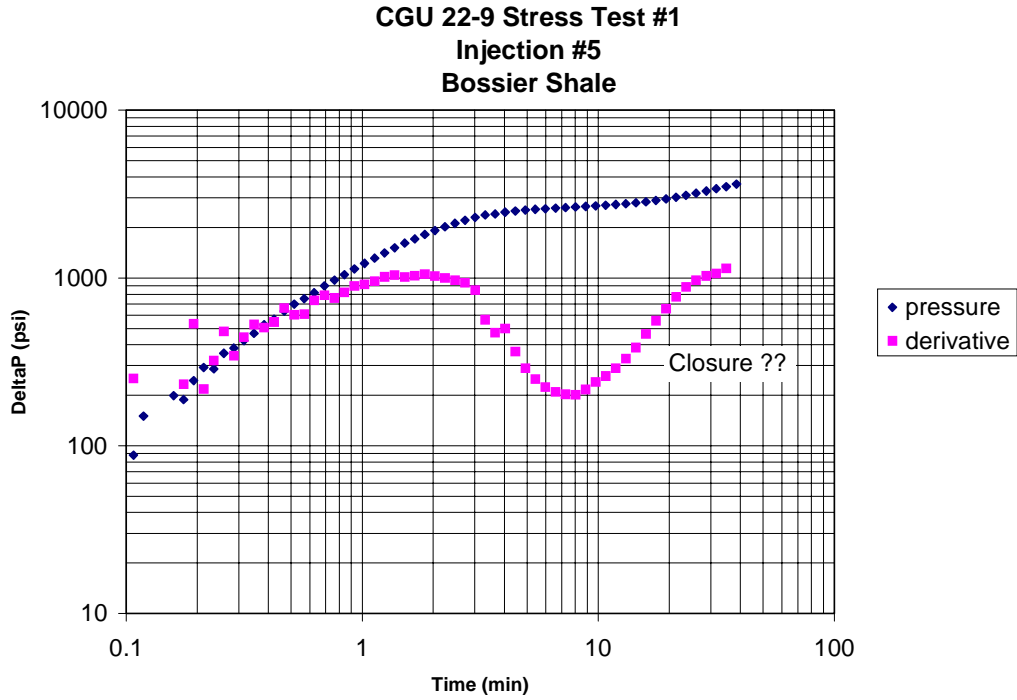


Figure 22. Injection #5: Log-log diagnostic plot of pressure decline

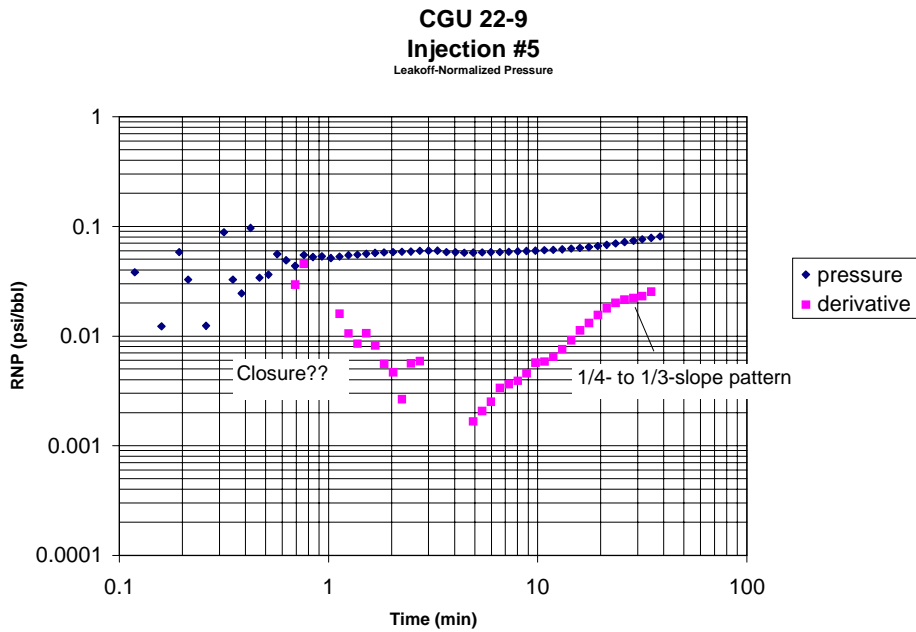
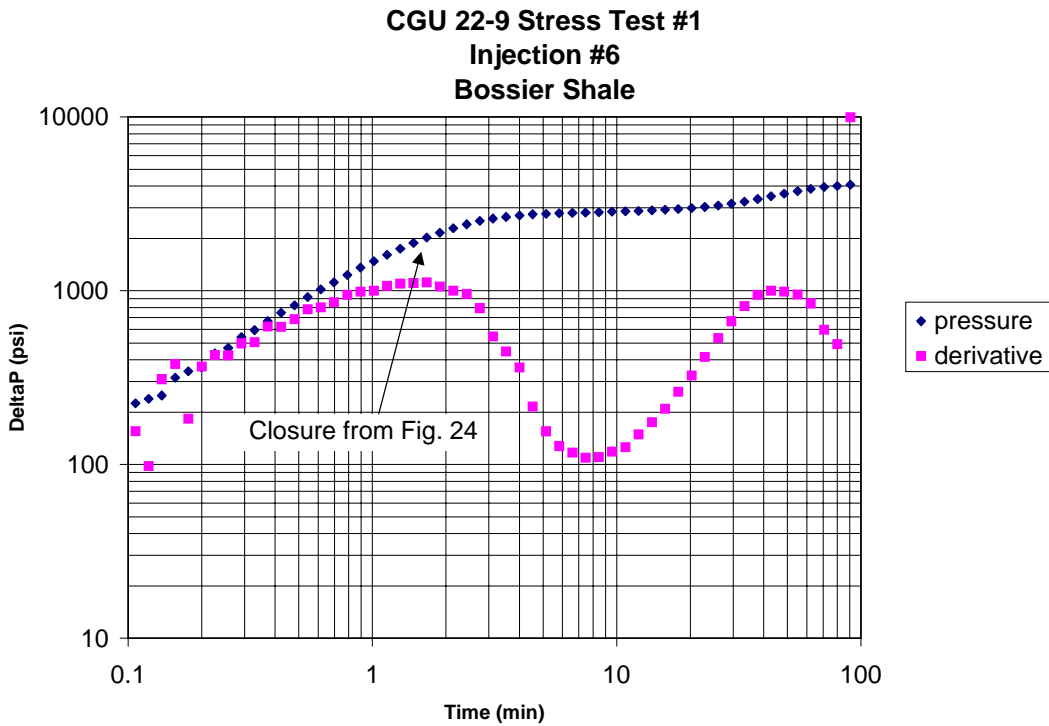


Figure 23. Injection #5: Leakoff-normalized diagnostic plot

*Injection #6*

As in Injection #5 the pump could not sustain any stable rate at maximum treating pressures. Figures 24 and 25 show the log-log diagnostic plots. Although the data is noisy, a brief period of linear flow can be detected up to about 1.5 minutes on the leakoff-normalized plot (Fig. 25). This would correspond to a closure pressure of 4,600 psi surface pressure (8,808 psi BHP) or 0.91 psi/ft. As in the previous injections complex reservoir flow is present in late time.



**Figure 24. Injection #6: Log-log diagnostic plot of pressure decline**

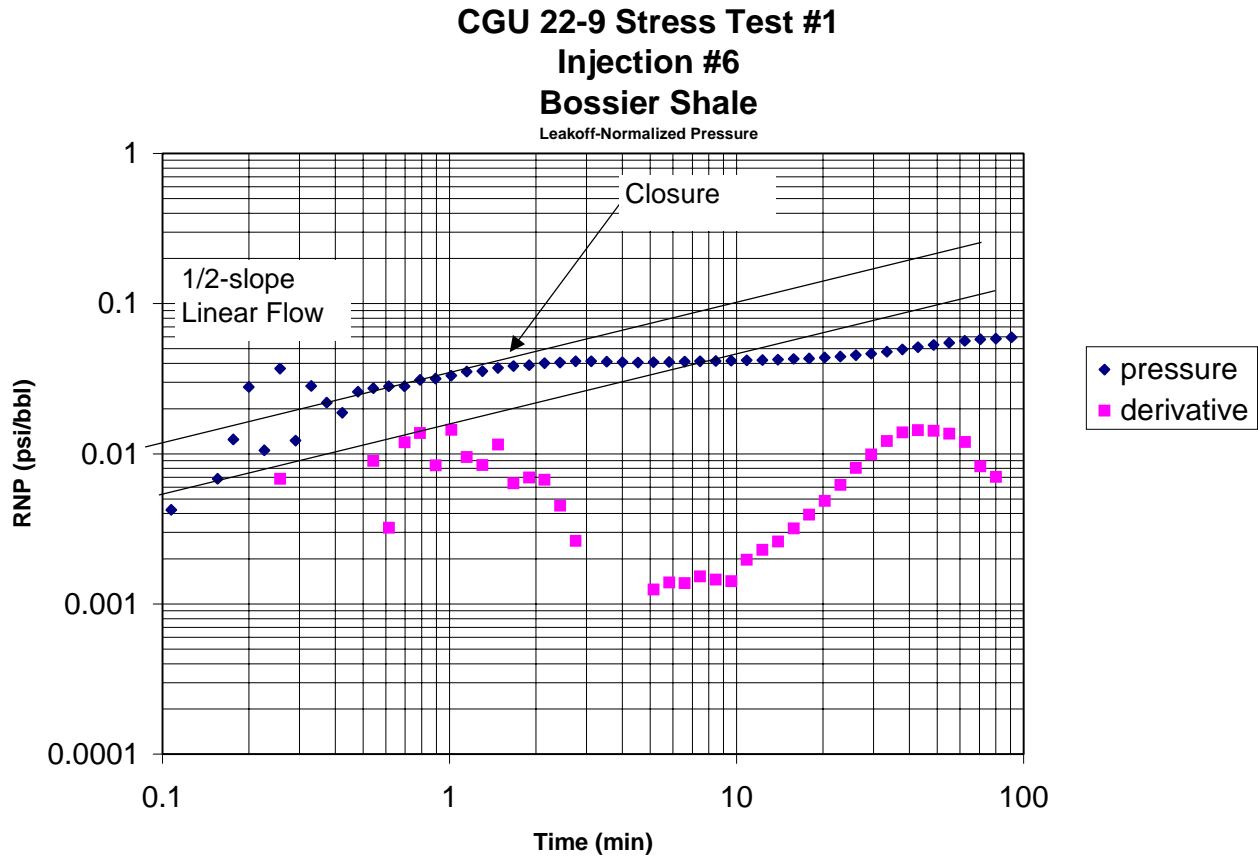


**Figure 25. Injection #6: Leakoff-normalized diagnostic plot**

### 3.1.2 Stress Test #2 – C-Lime (9,458’-9,460’)

Figure 26 shows the injection history. A total of four injections were performed. The flow pulse technique was performed on the third injection. Figure 27 shows the log-log diagnostic plot for Injection #1. Half-slope linear flow is present for about 0.5 minutes, where closure occurs at about 0.82 psi/ft stress gradient. The leakoff-normalized diagnostic plot shows the same linear flow pattern as the plot in Figure 27. Closure could not be clearly determined on the other injections due to lack of a linear flow regime. Similar to the first stress test in the Bossier shale, some sort of complex reservoir flow is present in late time indicated by the hump in the data and late-time 1/4-slope to 1/3-slope behavior.

### CGU 22-9 Stress Test#2 C-Lime

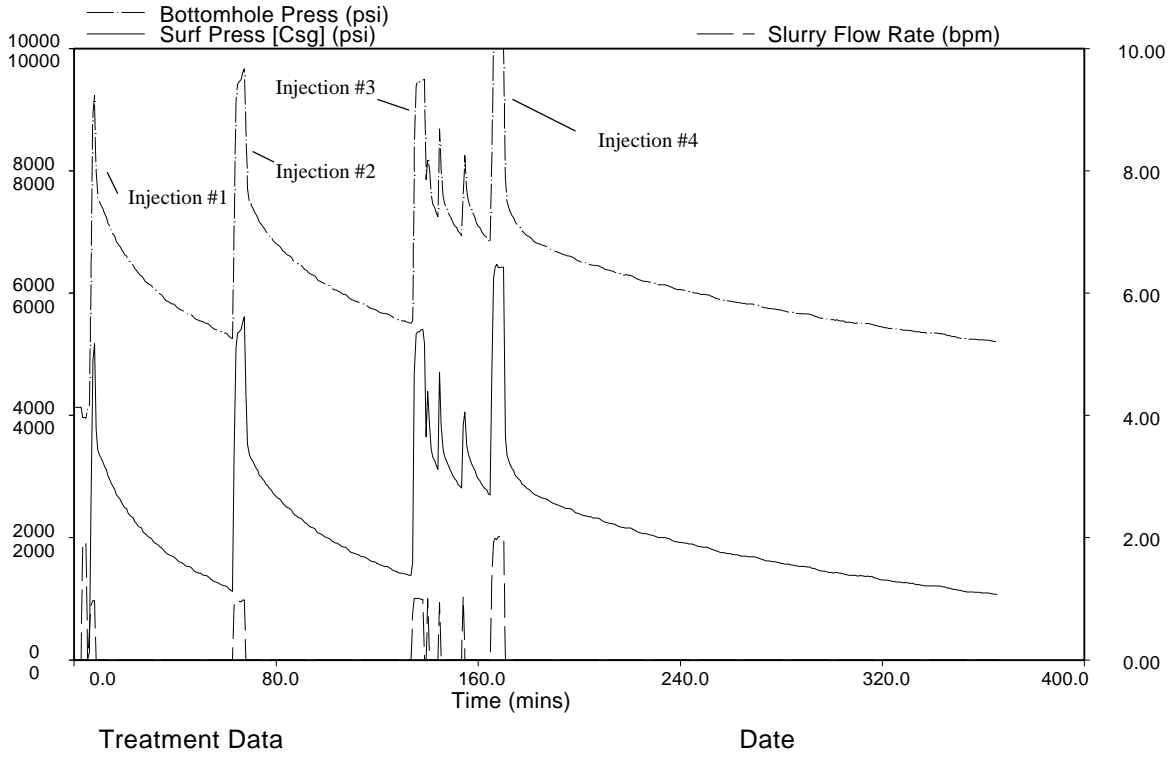
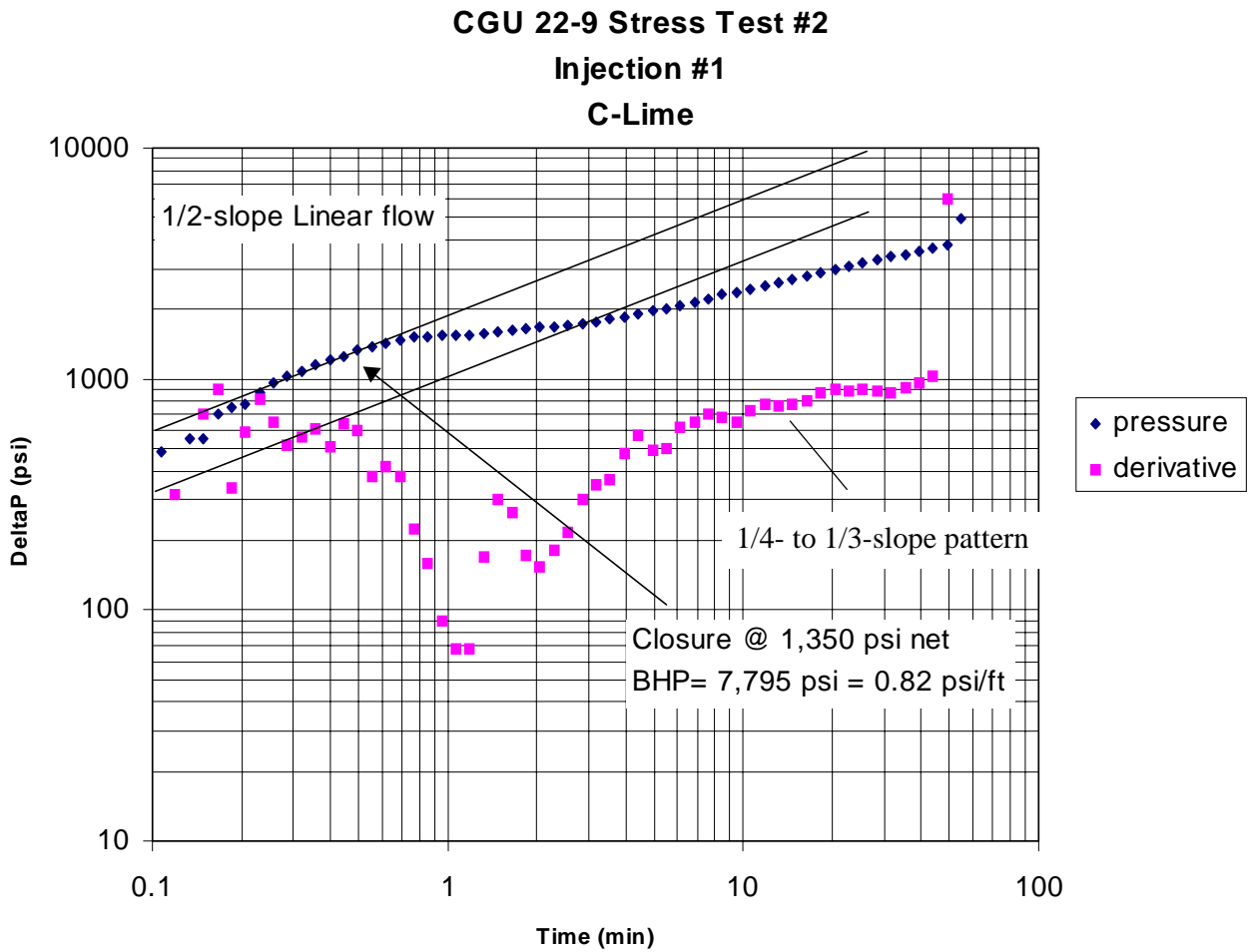


Figure 26. Stress Test #2 injection history



**Figure 27. Stress Test #2 - Injection #1: Log-log diagnostic plot of pressure decline**

**3.1.3 Stress Test #3 – Sexton Shale (9,318’-9,320’)**

Figure 28 shows the injection history. A total of four injections were performed. The flow pulse technique was performed on the third injection. Figure 29 shows the log-log diagnostic plot for Injection #1. Figure 30 shows the leakoff-normalized pressure on a log-log diagnostic plot. Half-slope linear flow is present for about 1 minute, where closure occurs at about 0.68 psi/ft stress gradient. For comparison, Figure 31 shows a straight-line closure analysis using a square-root of time plot. The closure analysis results of the subsequent injections confirm the 0.68 psi/ft stress gradient.

### CGU 22-9 Stress Test #3

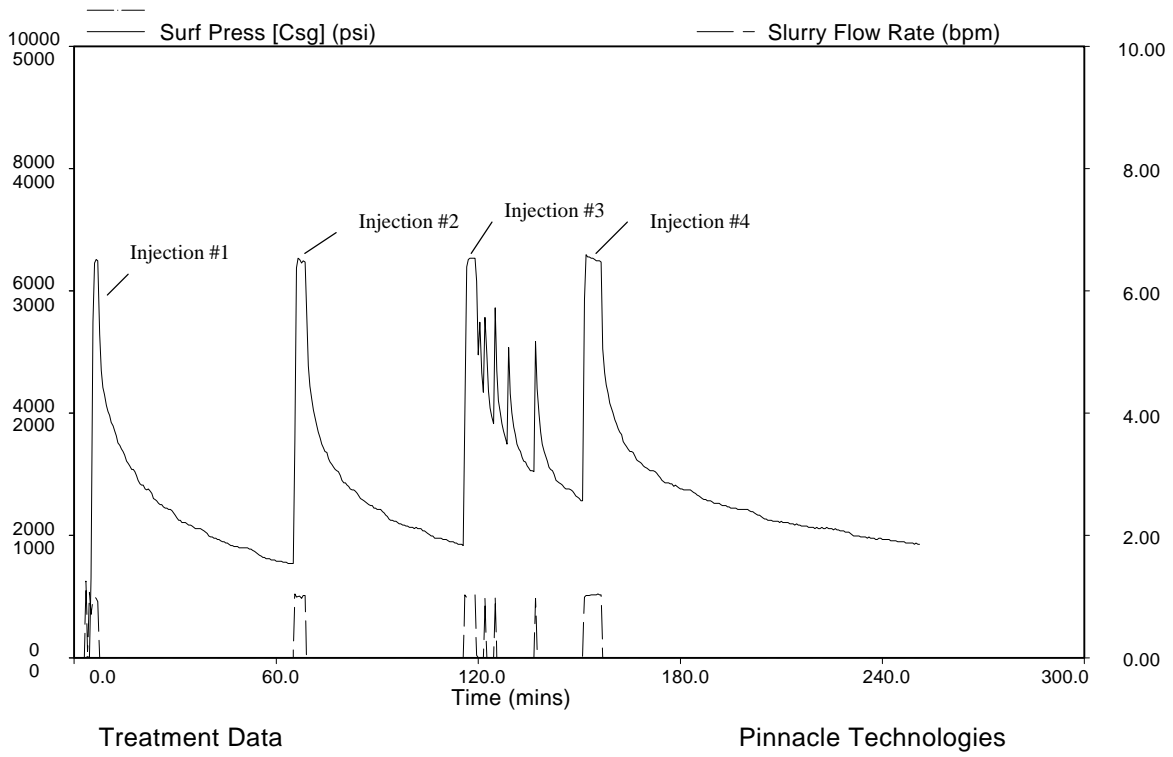
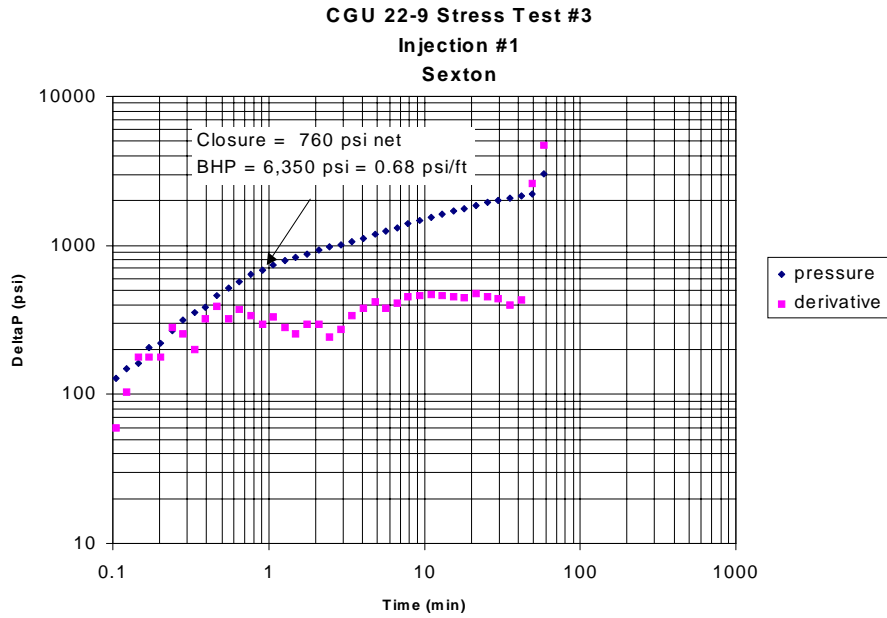
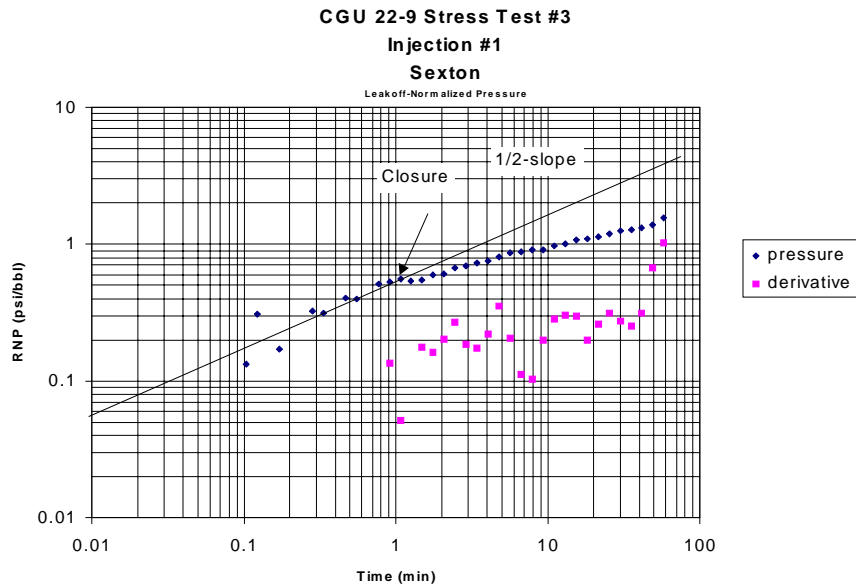


Figure 28. Stress Test #3 injection history



**Figure 29. Stress Test #3 - Injection #1: Log-log diagnostic plot of pressure decline**



**Figure 30. Stress Test #3 - Injection #1: Leakoff-normalized diagnostic plot**

### CGU 22-9 Stress Test #3

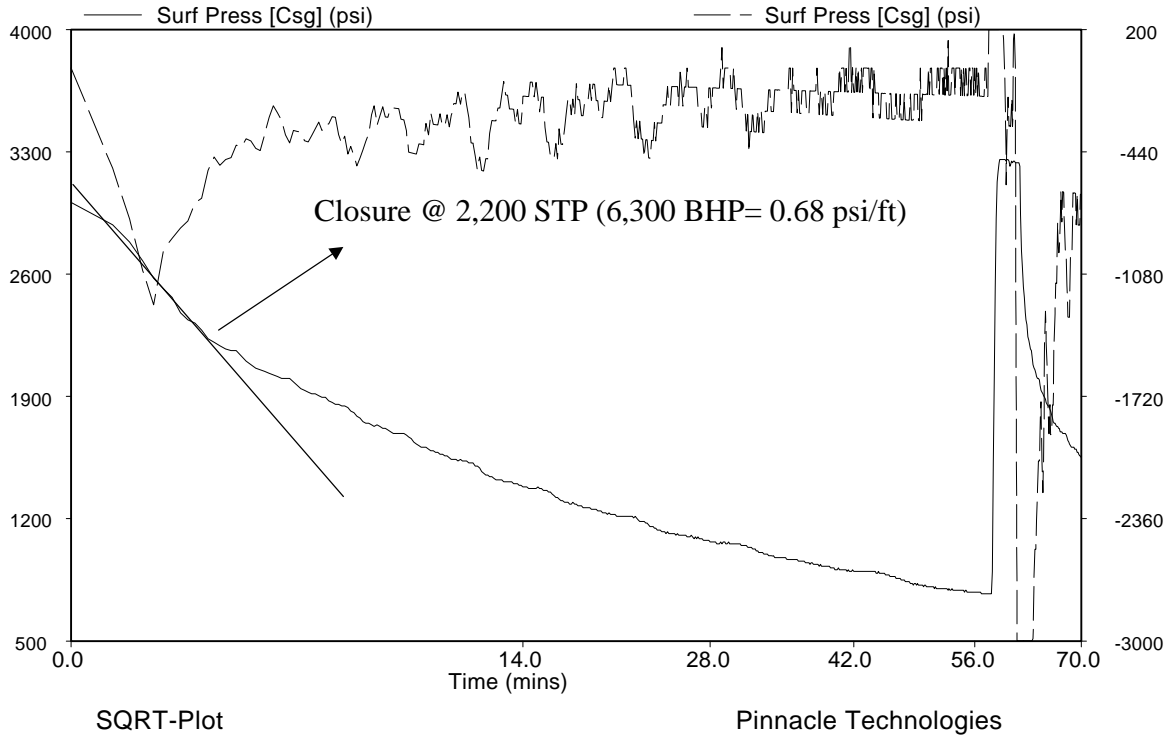


**Figure 31. Stress Test #3 – Injection #1: Square-root of time plot to determine closure pressure**

#### **3.1.4 Stress Test #4 – Davis (shale-sand sequence) (8,862’-8,864’)**

Figure 32 shows the injection history. A total of nine injections were performed. Figure 33 shows the log-log diagnostic plot for Injection #2 and Figure 34 for Injection #3. Both plots are very similar indicating a linear flow portion on the derivative. Closure occurs after about one minute at 0.57 psi/ft, where the data departs from half-slope linear flow behavior. The closure analysis results of the subsequent injections confirm a closure at about 0.57 psi/ft stress gradient.

CGU 22-9  
Stress Test #4: Davis (8,862'-8,864')

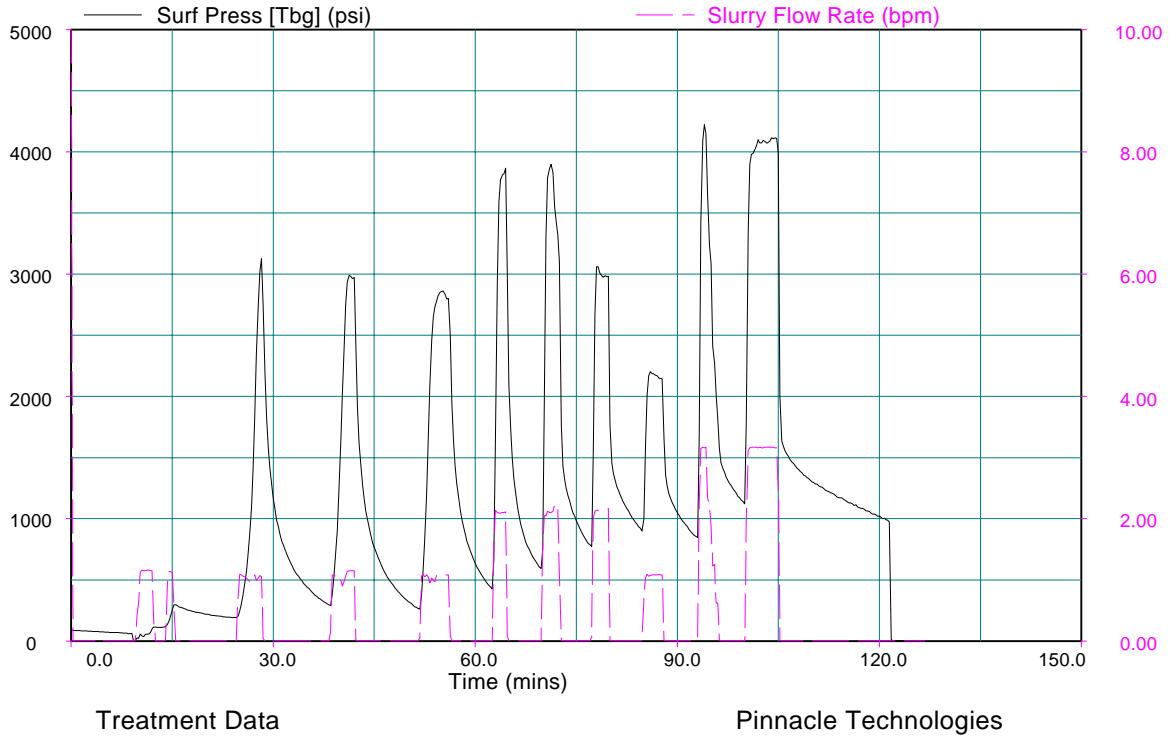


Figure 32. Stress Test #4 injection history

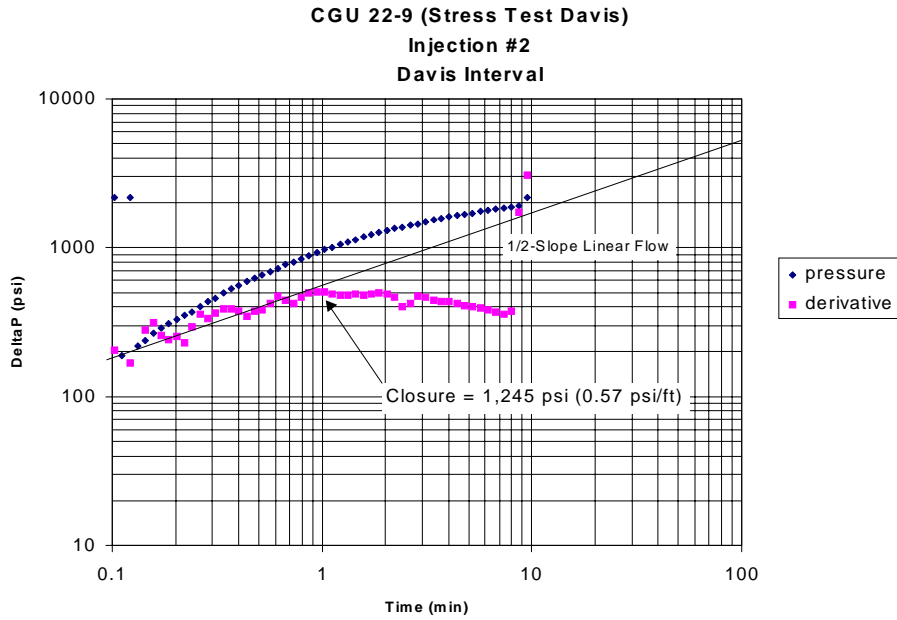


Figure 33. Stress Test #4 - Injection #2: Log-log diagnostic plot of pressure decline

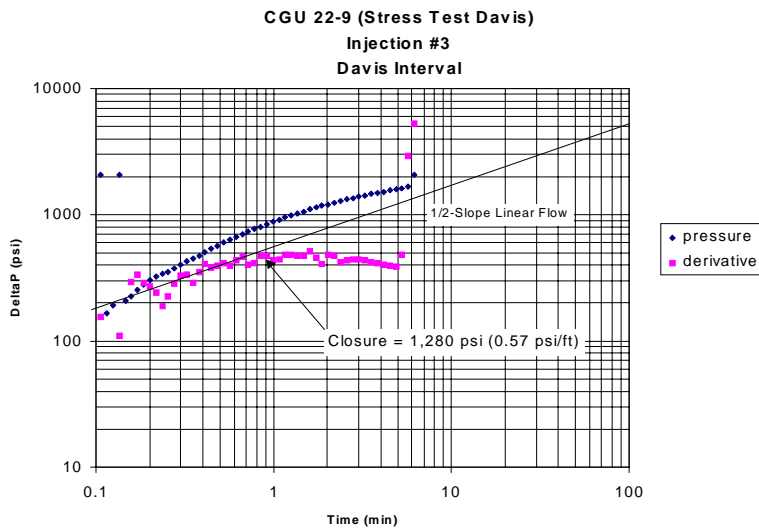


Figure 34. Stress Test #4 - Injection #3: Log-log diagnostic plot of pressure decline

# 4. Well Testing

Originally, we had planned to perform a total of five well tests, three prefrac and two postfrac tests. Unfortunately, we could not perform any of the prefrac buildup tests due to lack of gas inflow after perforating. This was probably caused by a combination of a complex wellbore configuration (two strings of pipe, strapped-on geophones and two cement sheaths could lead to substandard perforations) and significant reservoir depletion in some zones. The two postfrac pressure buildups (PBU's) were successful. Figure 35 shows the postfrac PBU test for Stage 1 in the Taylor sand. The well was flowing less than 100 MCFD at 300 psi surface pressure for about 27 days before it was shut in. The PBU shows a very short, low-conductivity fracture with the radial flow regime emerging within about 100 hours of buildup. The presence of radial flow enabled estimates of reservoir permeability and pressure. Reservoir pressure was found to be extremely low due to depletion (2,169 psi = 0.225 psi/ft). This severe depletion could also be the reason for the short effective fracture length due to substantial cleanup problems.

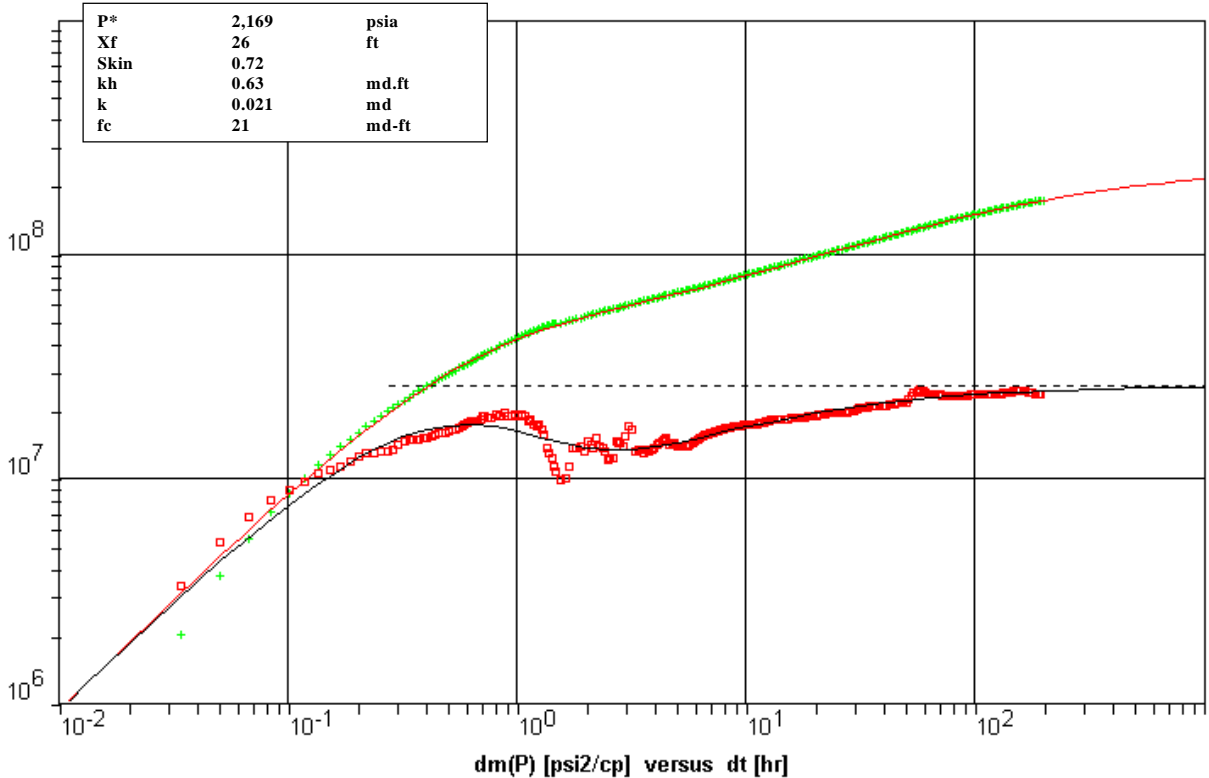
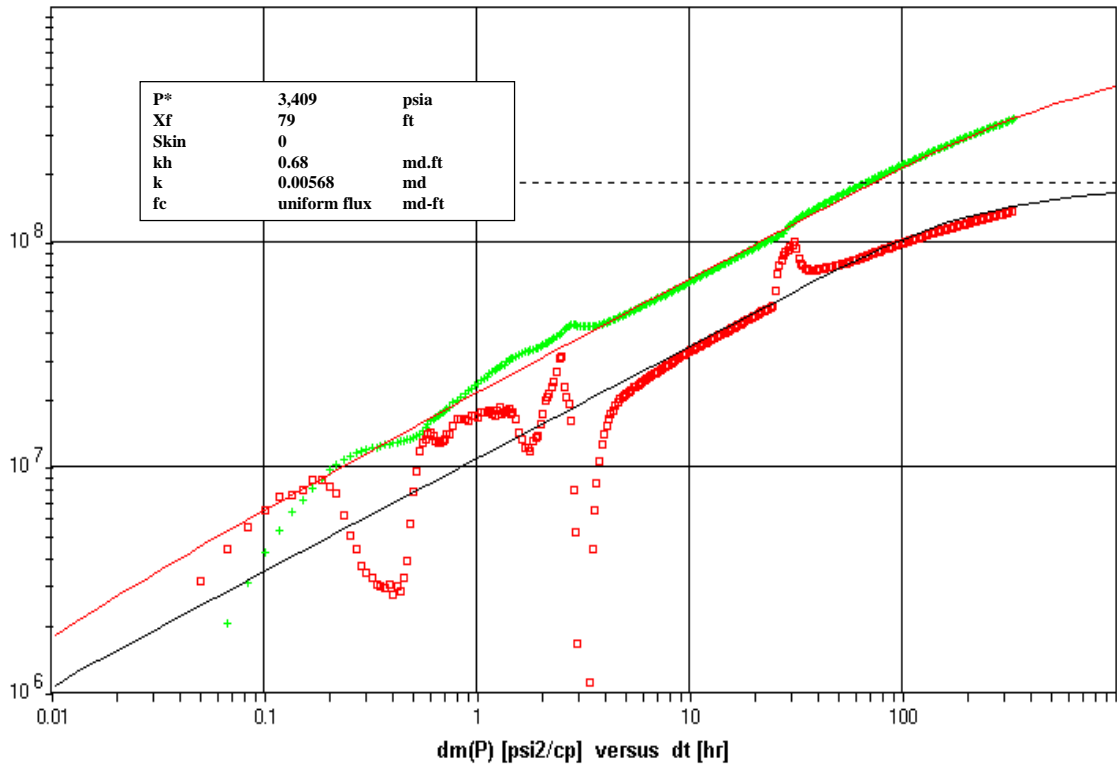


Figure 35. Postfrac pressure buildup test for Stage 1 – Taylor Sand

Figure 36 shows the postfrac PBU test for Stage 2 (Roseberry/Ardis Sand). The well was flowing about 240 MCFD at 280 psi surface pressure for about 65 days before it was shut in. This plot also shows a fairly short but highly conductive fracture. The quality of the fracture is definitely better than the one observed in Stage 1 (Taylor). Reservoir pressure is also higher at 3,423 psi but permeability appears to be somewhat lower than in the Taylor zone.



**Figure 36. Postfrac pressure buildup test for Stage 2 – Roseberry/Ardis Sands**

## 5. Production Log Results

Table 6 is a summary of the flow contributions from each perforated interval/stage. The production log was run in conjunction with the tracer log using the Completion Profiler™ by ProTechnics. The majority of the production (50%) is coming from the uppermost Stage 4 interval. The total well production was about 1,140 MCFD at the time of the production log run. The tracer and production is shown in **Appendix D**.

**Table 6. Summary of Production Log Results**

Stage	Gas Rate (MCFD)	Percentage
<b>Total</b>	<b>1136</b>	<b>100%</b>
Stage 1 9,584'-9,614'	162	14%
Stage 2 9,150'-9,272'	156	14%
Stage 3 8,935'-9,050'	257	23%
Stage 4 8,645'-8,779'	561	49%

## 6. Fracture Modeling

Fracture modeling was performed using the 3-D fracture model FracProPT™. The stress profile was created using the measured values from stress tests and minifrac diagnostic injections in the pay zones (Figure 4). Table 6 summarizes all the pertinent results and treatment data of all 4 stages in the CGU 22-9. The CGU 22-9 well log showing stress test and frac stage intervals is shown in **Appendix E**.

**Table 7 - Summary of CGU 22-9 Fracture Engineering Results**

Stage	Net Pressure (psi)	Fracture Half-Length (ft)	Propped Half-Length (ft)	Fracture Height (ft)	Propped Height (ft)	Proppant Concentration in fracture (lbs/ft <sup>2</sup> )
#1 (Taylor) 9,584'-9,690'	1,480	1,758	1,500	159	159	0.15
#2 (Roseberry/Ardis) 9,150'-9,272'	850	983	983	323	323	0.10
#3 (Bolinger/Justice/E) 8,935'-9,070'	570	476	476	442	442	0.10
#4 (Bodcaw/Vaughn) 8,645'-8,779'	600	596	596	464	464	0.11

Stage	Slurry Volume (bbls)	Sand (klbs)	Injection Rate (bbls/min)	Closure Stress (psi/ft)	Efficiency Mini/Main (%)	Leakoff Coefficient (ft/min <sup>1/2</sup> )
#1 (Taylor) 9,584'-9,690'	4118	48	25	0.58	77 / 51	0.00085
#2 (Roseberry/Ardis) 9,150'-9,272'	4116	52	25	0.61	80 / 54	0.00053
#3 (Bolinger/Justice/E) 8,935'-9,070'	4539	51	25	0.57	58 / 40	0.00068
#4 (Bodcaw/Vaughn) 8,645'-8,779'	4797	32	30	0.55	50 / 48	0.00153

Figures 37 to 54 show treatment data, net pressure matches, model fracture geometries and minifrac pressure decline analysis plots for all four stages in the CGU 22-9. Closure pressure was estimated from log-log diagnostic plots, in some cases square-root of time plots and one pump-in/flowback test. In general, net pressures are above 500 psi at the end of the job with confined fracture growth in the Taylor zone and less confined growth in the Upper Cotton Valley. Due to the complex wellbore configuration all treatments had unusually high perforation friction. In some cases perforation friction exceeded 1,000 psi at 25 bpm. Table 7 summarizes the stepdown analysis results to estimate perforation and near-wellbore friction.

**Table 8. Results of stepdown tests**

<b>Stage</b>	<b>Perf. Friction (psi)</b>	<b>Near-Wellbore Friction (psi)</b>	<b>Injection Rate (bbls/min)</b>
#1 (Taylor) 9,584'-9,690'	625	184	25
#2 (Roseberry/Ardis) 9,150'-9,272'	1,182	166	25
#3 (Bolinger/Justice/E) 8,935'-9,070'	1,530	0	25
#4 (Bodcaw/Vaughn) 8,645'-8,779'	174	0	30

CGU 22-9  
Stage No.1

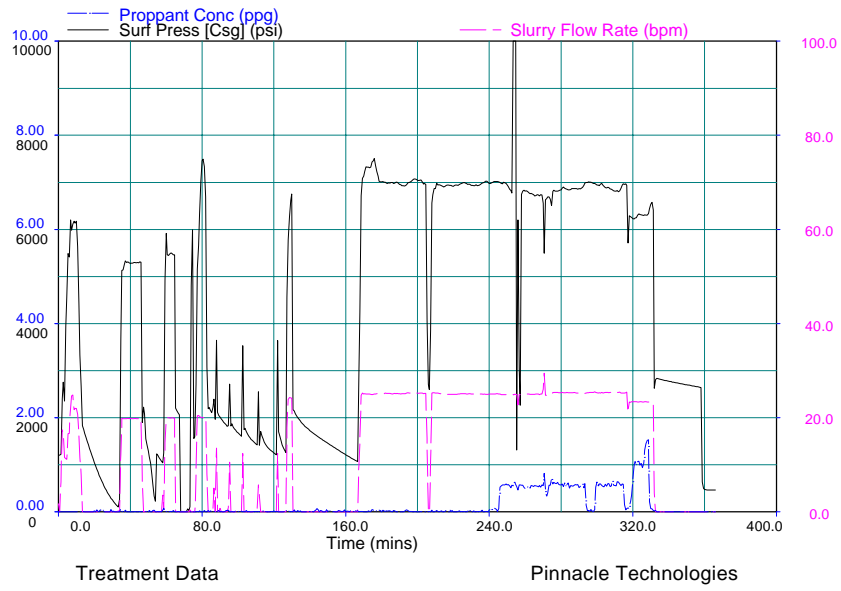


Figure 37. Treatment data: CGU 22-9 Stage 1

CGU 22-9  
Stage No.1

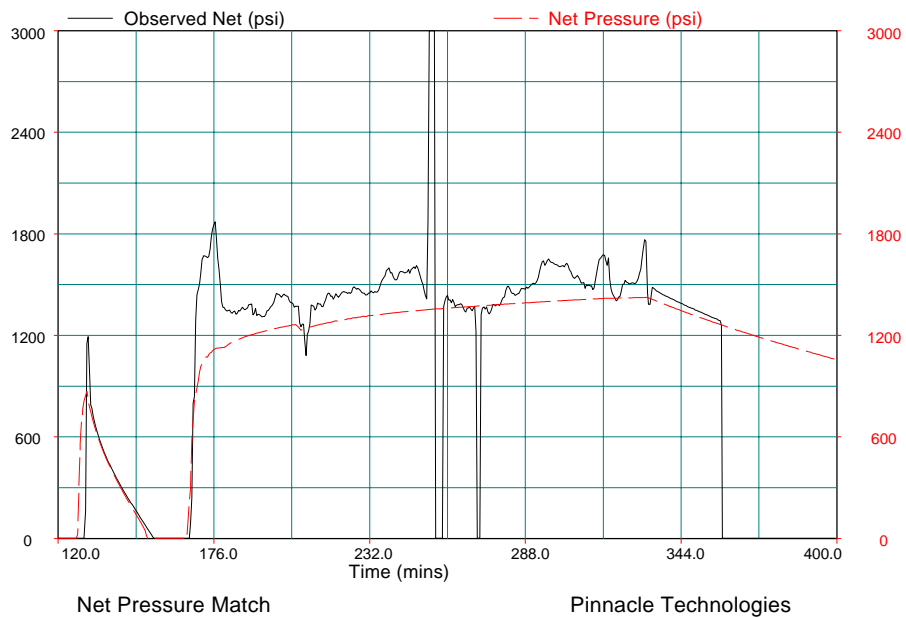


Figure 38. Net Pressure Match: CGU 22-9 Stage 1

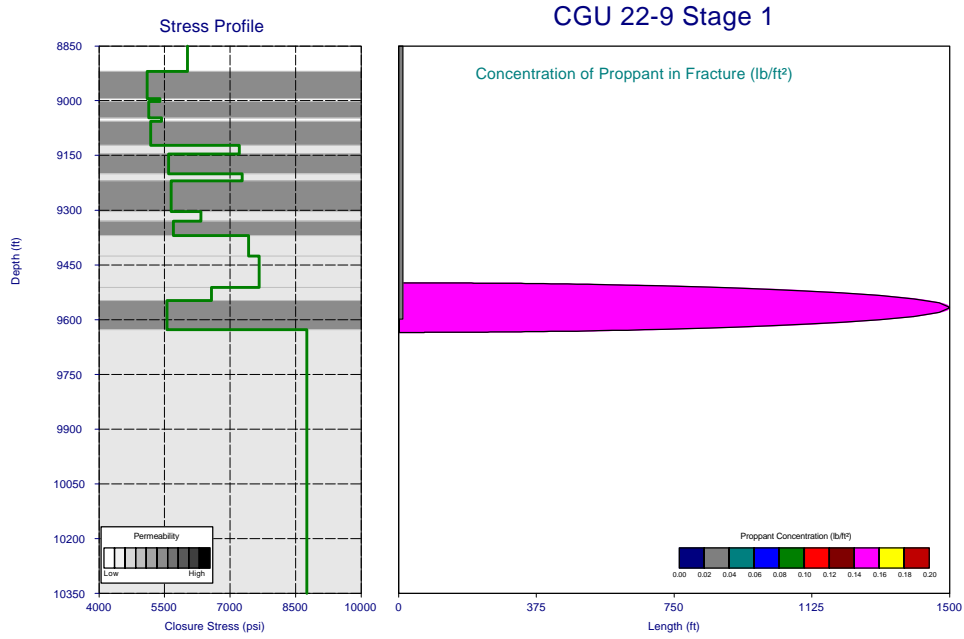


Figure 39. Fracture Geometry: CGU 22-9 Stage 1

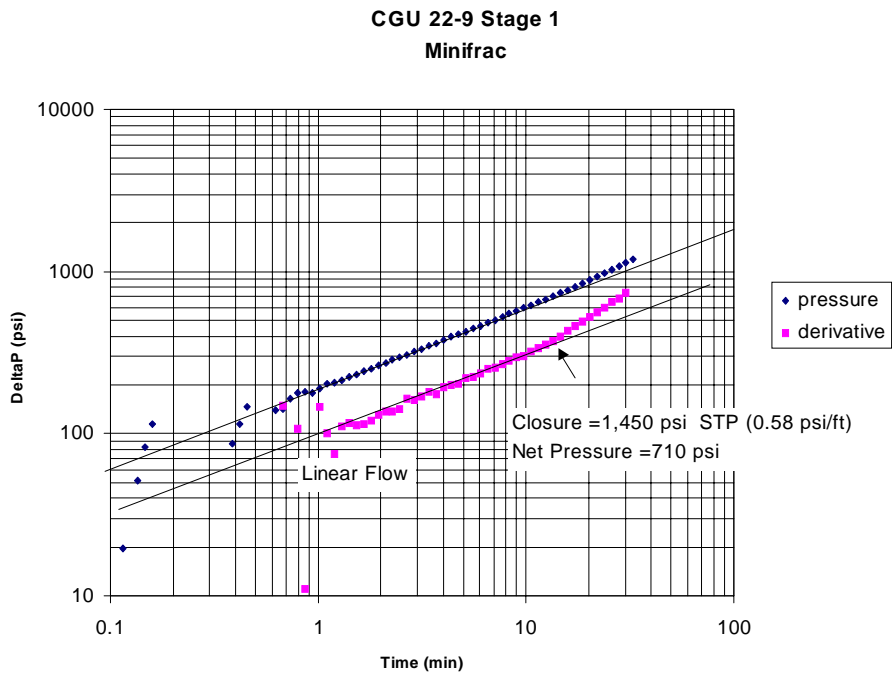
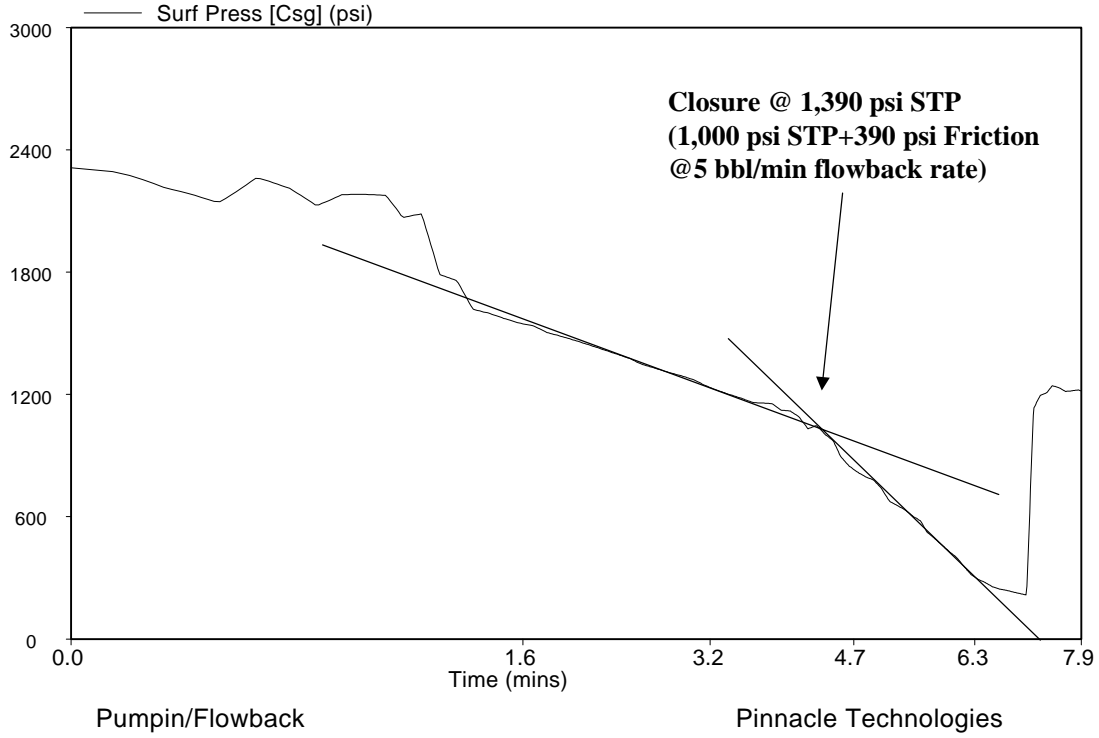


Figure 40. Estimating closure pressure from log-log diagnostic plot: Stage 1

CGU 22-9  
Stage No.1



**Figure 41. Estimate of closure from pump-in/flowback test confirms log-log plot estimates: Stage 1**

CGU 22-9  
Stage No.2

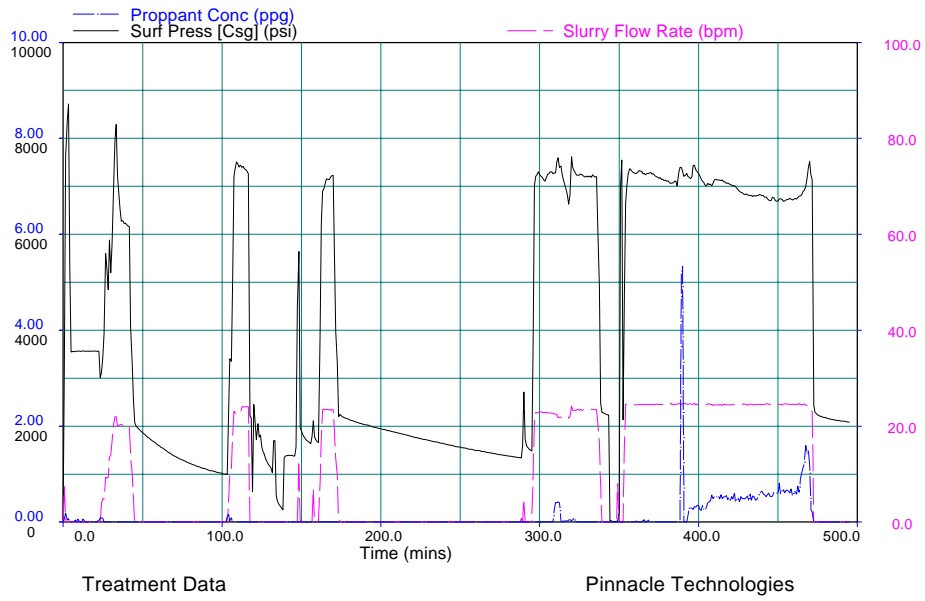


Figure 42. Treatment data: CGU 22-9 Stage 2

CGU 22-9  
Stage No.2

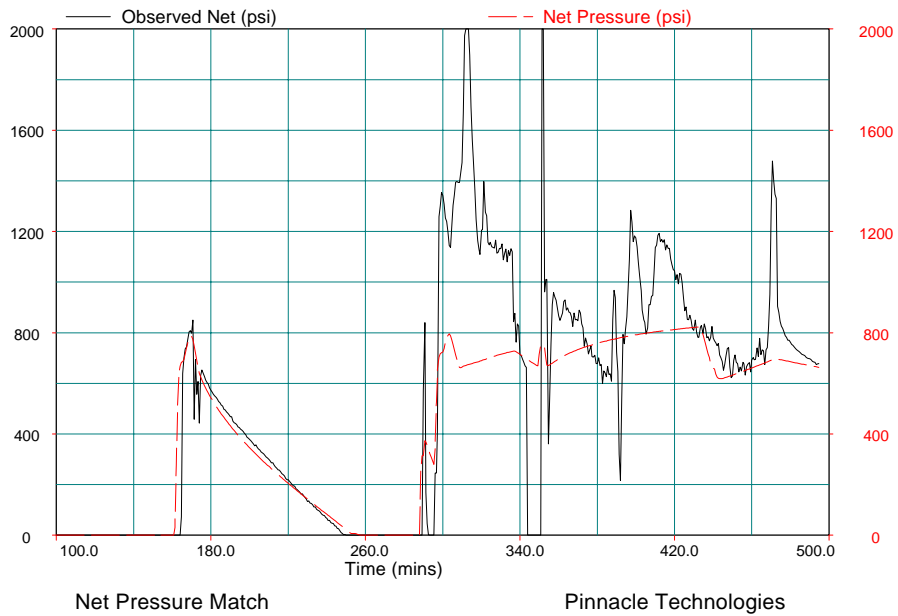


Figure 43. Net Pressure Match: CGU 22-9 Stage 2

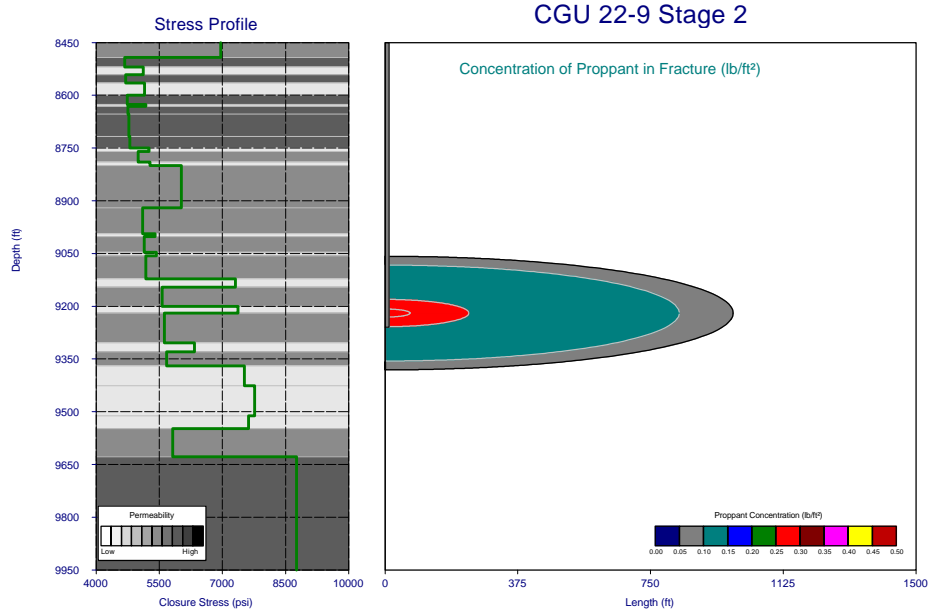


Figure 44. Fracture Geometry: CGU 22-9 Stage 2

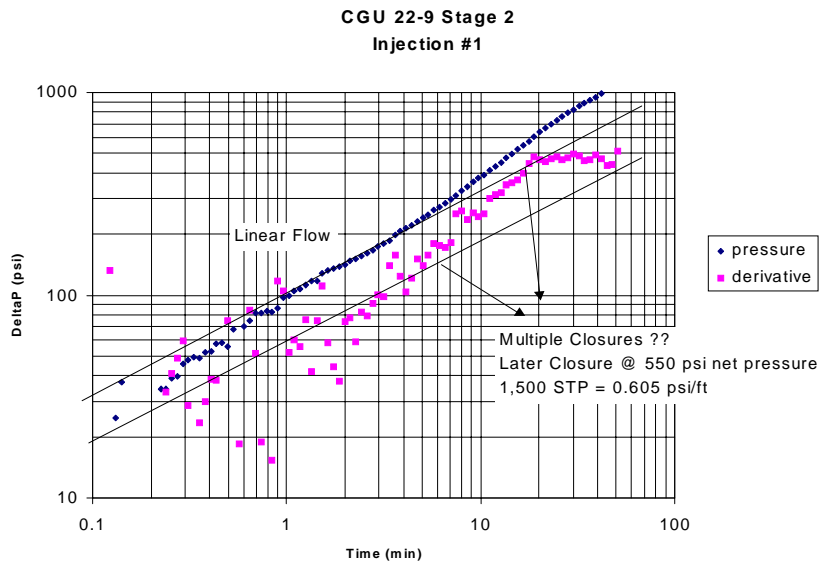


Figure 45. Estimating closure pressure from log-log diagnostic plot: Stage 2

CGU 22-9  
Stage No.2

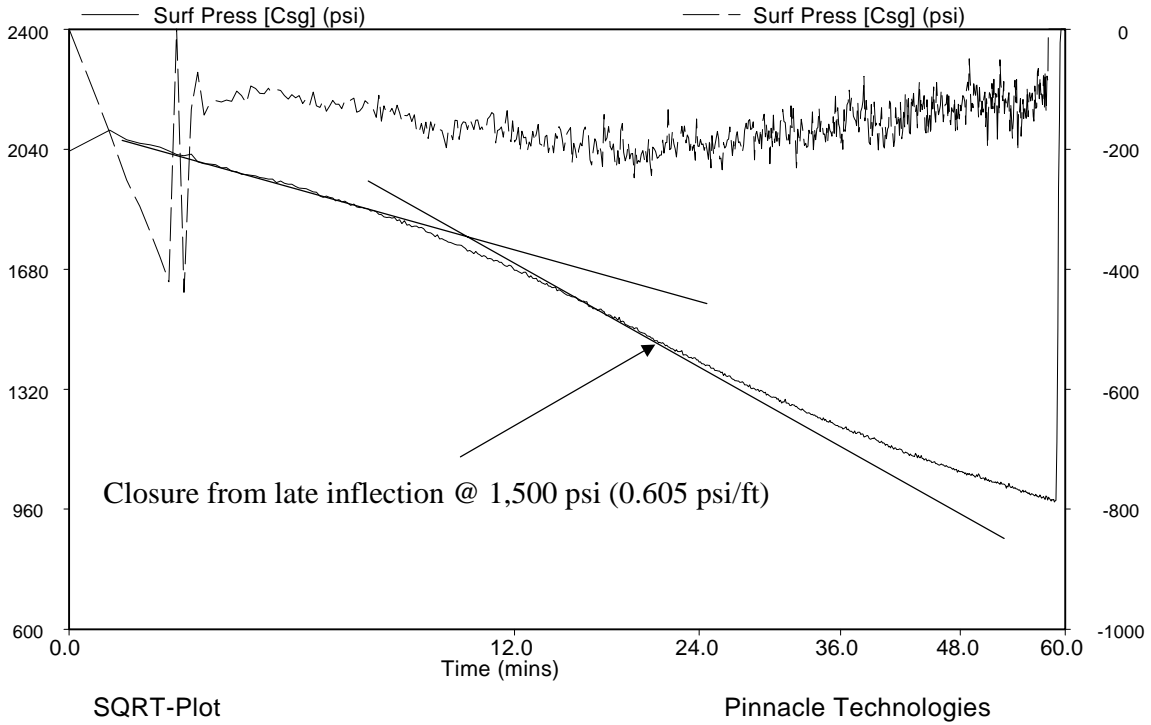


Figure 46. Estimating closure pressure from square-root of time plot: Stage 2

CGU 22-9  
Stage No.3

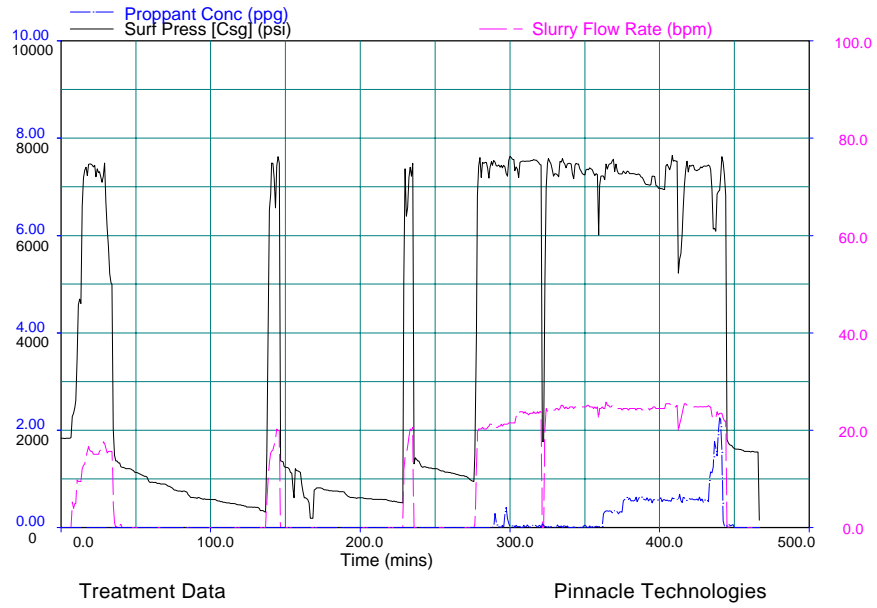


Figure 47. Treatment data: CGU 22-9 Stage 3

CGU 22-9  
Stage No.3

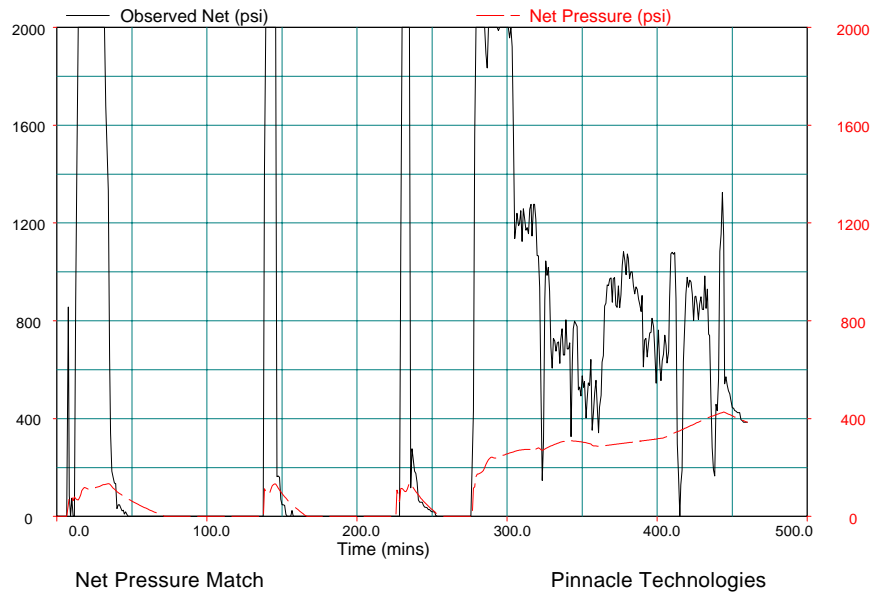


Figure 48. Net Pressure Match: CGU 22-9 Stage 3

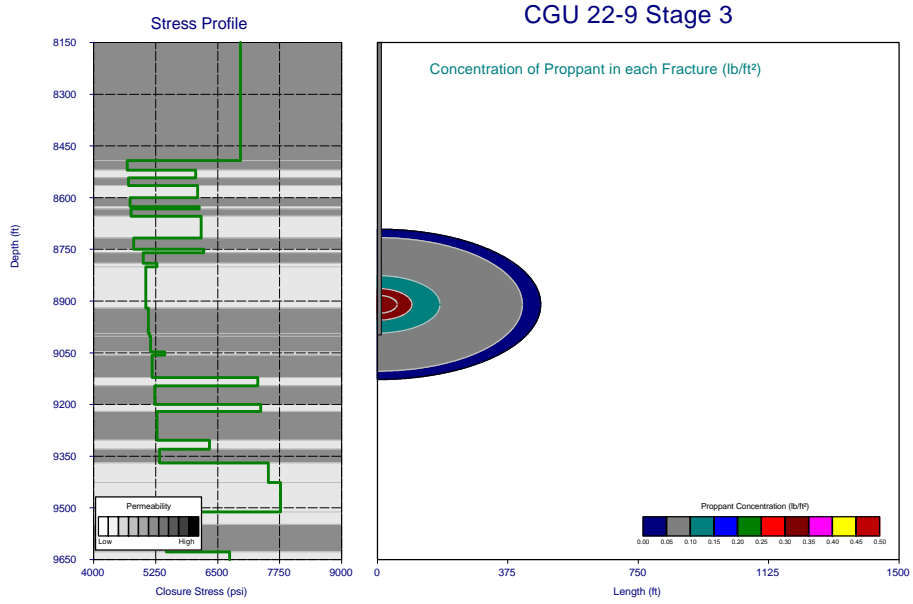


Figure 49. Fracture Geometry: CGU 22-9 Stage 3

CGU 22-9  
Stage No.3

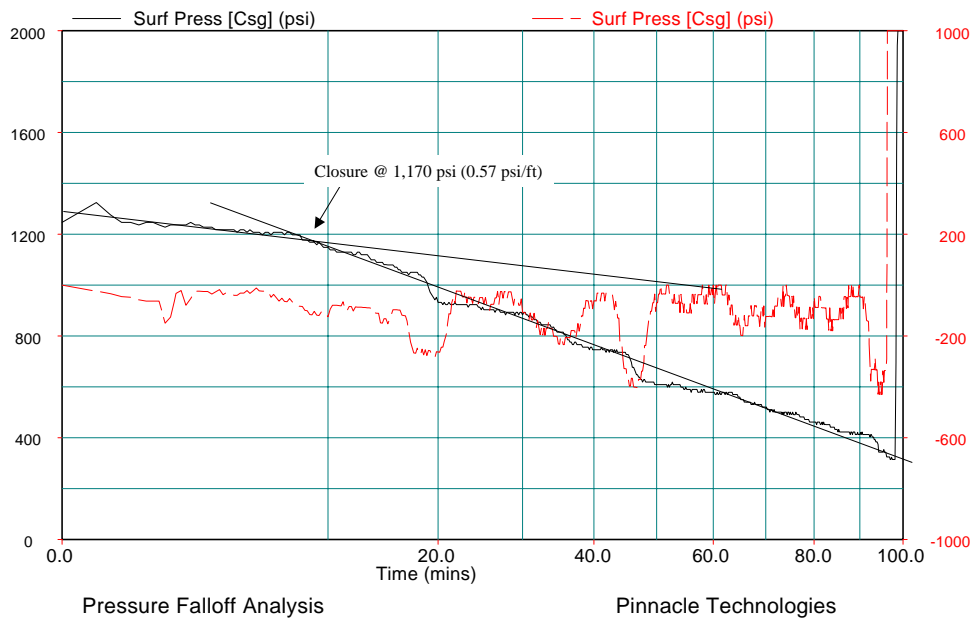


Figure 50. Estimating closure pressure from square-root of time plot: Stage 3

CGU 22-9  
Stage No.4

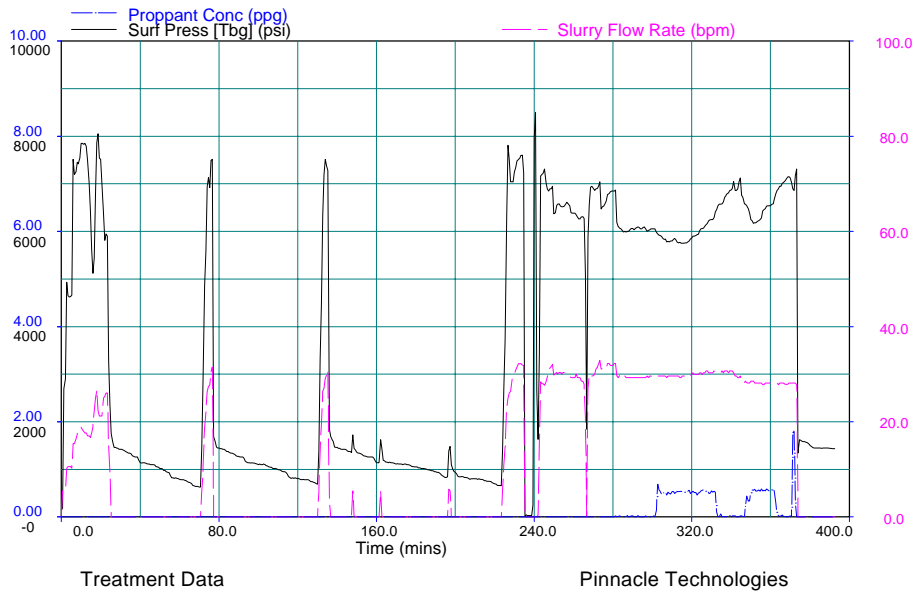


Figure 51. Treatment data: CGU 22-9 Stage 4

CGU 22-9  
Stage No.4

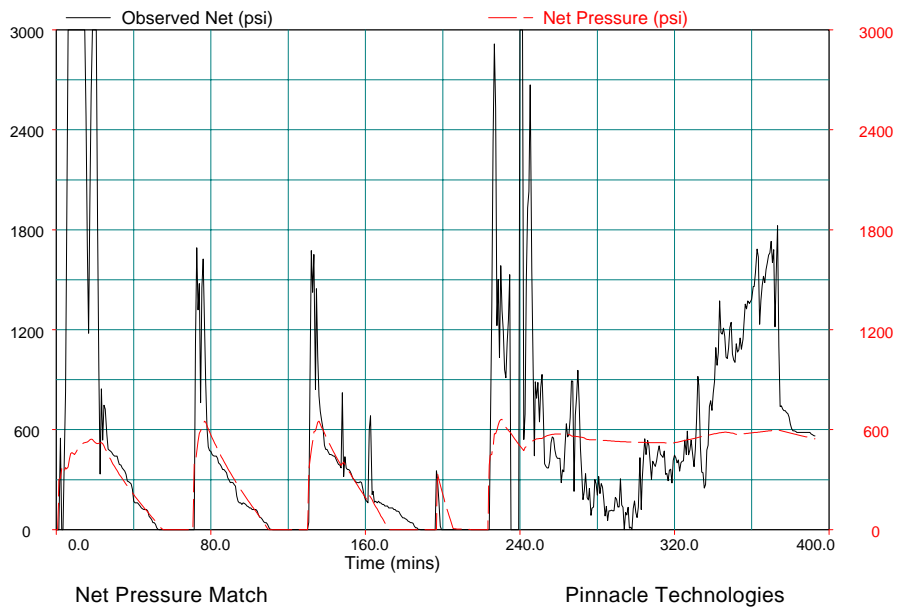


Figure 52. Net Pressure Match: CGU 22-9 Stage 4

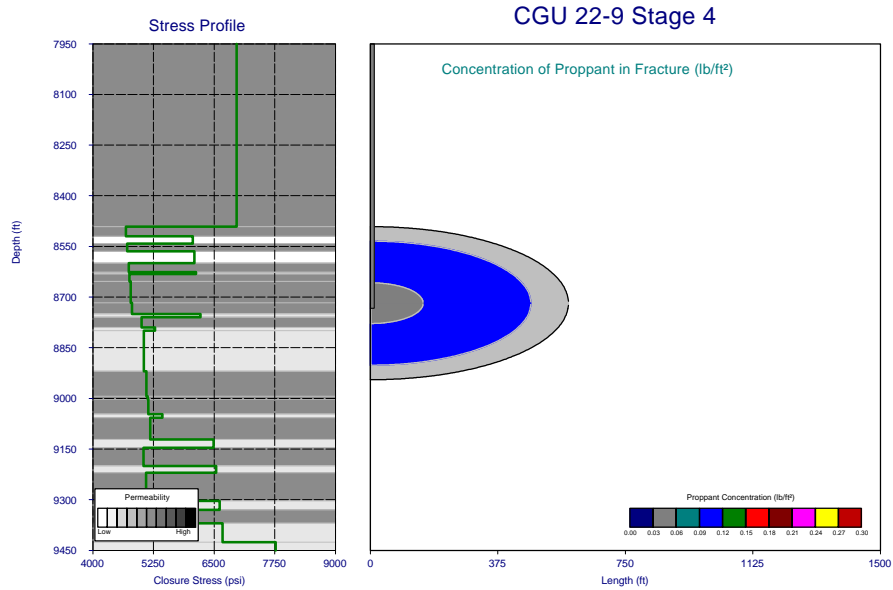


Figure 53. Fracture Geometry: CGU 22-9 Stage 4

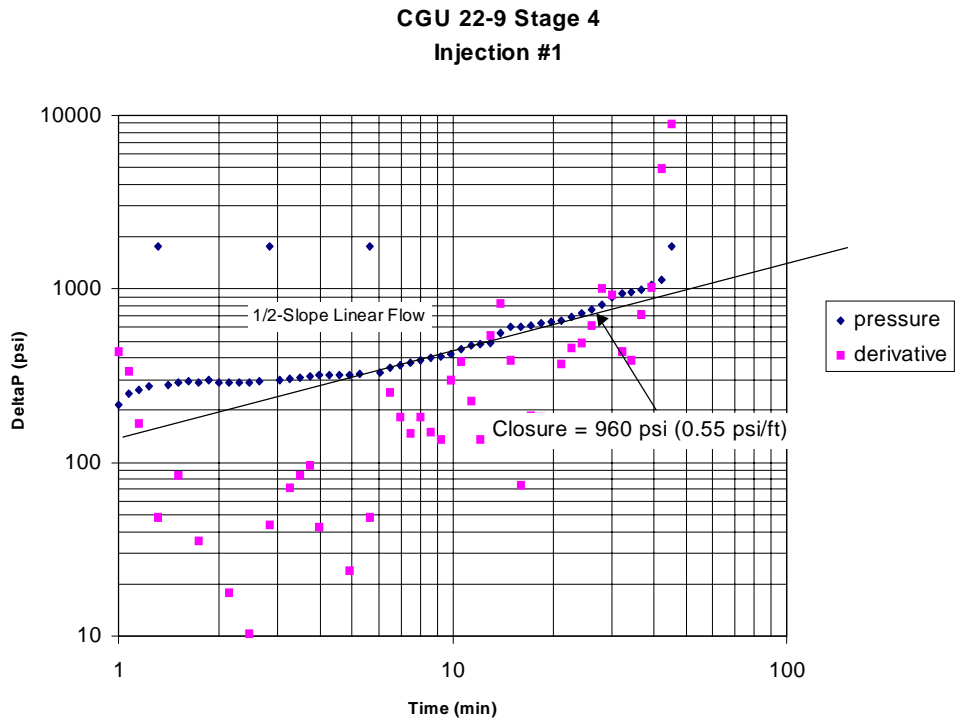
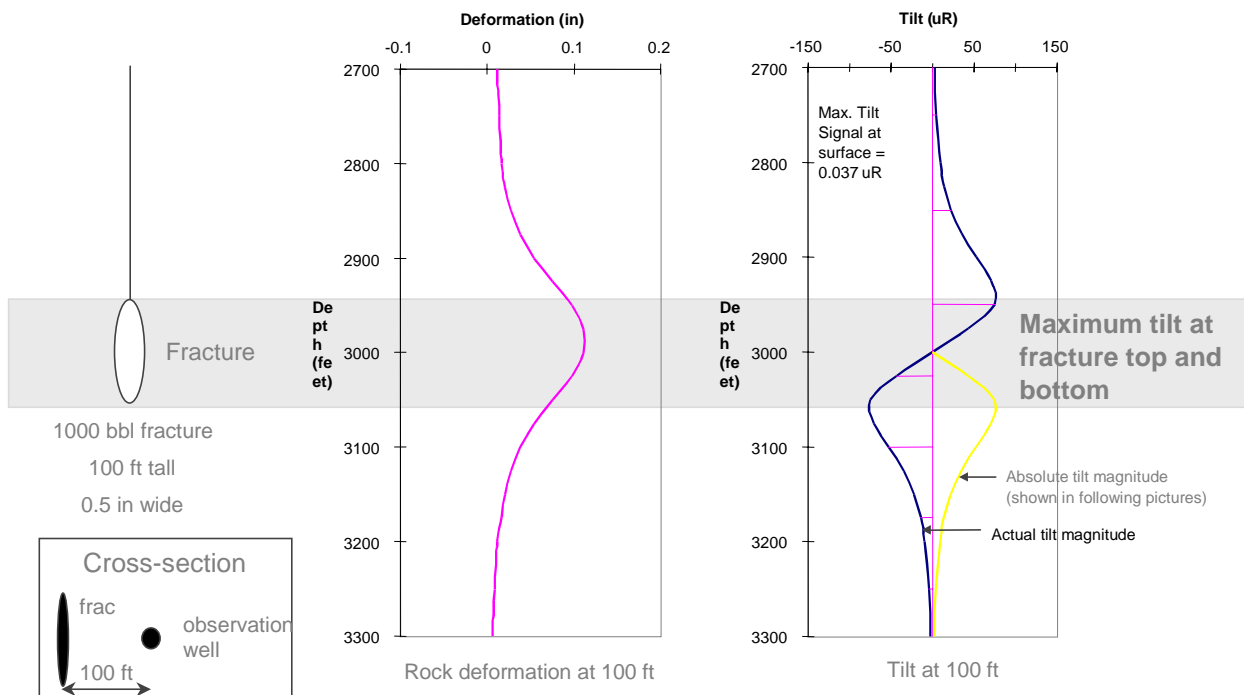


Figure 54. Estimating closure pressure from log-log diagnostic plot: Stage 4

## Appendix A – Overview of Downhole Tiltmeter Fracture Mapping

Downhole tiltmeters operate on exactly the same principle as surface tiltmeters. Placing tiltmeters in a wellbore offset from the treatment well, however, yields significantly different data. The tiltmeters in the wellbore are extremely sensitive to fracture height. As a hydraulic fracture is created, the formation nearby is pushed away from the fracture faces. Directly across from the center of the fracture face, a tiltmeter will detect no movement because the motion is purely lateral. Above the center of the fracture, the formation (and the offset wellbore) will tilt in one direction. Below the center of the fracture, the formation will tilt in the opposite direction. It turns out that, when the offset well is close to the treatment well, the points of maximum tilt coincide with the top and bottom of the created fracture.

Plots of raw tiltmeter data show tilt versus time for each of the tiltmeters in an offset well. The change in the magnitude of tilt during the treatment is extracted and plotted versus the tiltmeter depth. The model then places a fracture at the appropriate depth along the treatment wellbore having a dominant orientation determined by the surface tiltmeters. The dimensions of height and length of the modeled fracture are then changed to obtain an optimum fit between the measured and theoretical tilt signals in the offset well. If needed, a secondary (smaller) fracture is added to the model to obtain a best fit to the data.



**Figure 55: Theoretical deformation pattern from downhole tiltmeters during a fracture treatment.**

There is currently no mechanism to determine the orientation of the downhole tiltmeters. However, orientation can be inferred once a fracture is mapped. By assuming one of the diagnostic fractures is located close to the treatment well perforations, one can determine the orientation of each tool for each stage. For those stages, where a good fit between the observed and theoretical tilt signals was elusive, the orientations of the tools were mapped, at which point it became easier to determine which tiltmeters were located at the bottom of a fracture and which were located at the top of a fracture.

Figure 55 shows the theoretical physical deformation created by a fracture and the gradient of deformation, or the tilt. The plots of tilt versus depth for the real data fit a theoretical best-fit line to the actual data points measured.

A single downhole tiltmeter array is used to obtain the tilt signals since the main goal of the downhole tiltmeter mapping was to determine fracture height. Fracture length was deemed less important. Red lines in the graphic on the right of Figure 55 show the spacing between the tiltmeters. The array was positioned in the observation well so that middle of the array was close to the same depth as the center of the perforated interval in the treatment well for each stage.

## Appendix B. High Downhole Temperatures and the Impact on Downhole Tiltmeter Fracture Mapping

Use of downhole tiltmeters in a 239°F environment posed some technological challenges, which had to be overcome to allow an accurate analysis of the tiltmeter data. Problems, which had to be addressed included wireline electrical integrity and heat induced noise within the raw tiltmeter data.

Thermometers within each tiltmeter on our two downhole arrays reported temperatures between 239°F and 245°F at the operating depths of 7600'- 8300' within observation wells CGU 22-4 and CGU 20-6. This heat introduced noise into the data reported by the tiltmeter arrays. Fortunately this noise was very regular in nature allowing its removal using simple and effective filtering techniques (Figure 56).

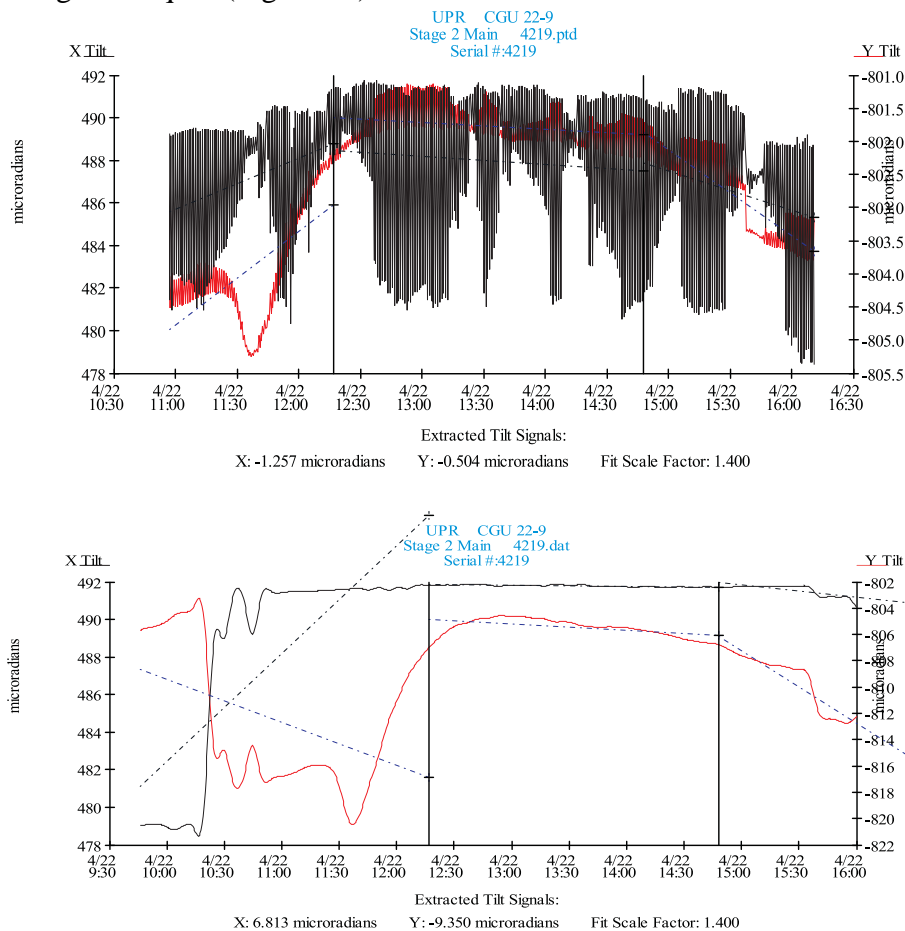


**Figure 56. Examples of raw downhole tiltmeter data containing heat-induced noise (top graph) and filtered tiltmeter responses (bottom graph). Extreme regularity of the noise spikes allowed effective filtering of the data and a successful analysis of the downhole tilt data.**

---

## Appendix C. Use of Well Testing Diagnostic Plots to Determine Fracture Closure Pressure

Mathematically, a straight-line on a square-root of time plot must be a half-slope straight-line on a log-log plot. In well test analysis of fractured wells, log-log diagnostic plots of the pressure change and log-derivative of pressure change are used for flow regime identification. The diagnostic strength of this technique is that the log-derivative is unmistakably clear about the character of the pressure response. A half-slope straight line on both the pressure change and log-derivative of the pressure change indicates reservoir linear flow into/or out of a fracture. The pressure decline after fracturing must also be characterized by linear flow of an open fracture, which is closing and leaking off into the formation. As soon as the fracture closes fully, linear flow should cease and system compliance will change. This is the reason why the industry frequently uses square-root of time plots (or G-function plots, which correct for different leakoff ages within the fracture) to identify linear flow as a straight-line of the falloff data. A departure from this straight-line would be the end of linear flow, which is equivalent to fracture closure.

However, the square-root of time plot has pitfalls. More often than not a straight-line is drawn through data that appears to be straight (up to the Engineer's judgement) but in reality it is a continuous curve, which is clearly evident on the log-log plot as not being half-slope. A square-root of time plot should only be used after linear flow has been properly identified on the log-log diagnostic plot. If there is no half-slope behavior on the log-log diagnostic plot then no dominant linear flow is present and straight-lines on square-root of time plots are arbitrary when estimating closure.

An additional pitfall of the square-root of time analysis is that leakoff does not happen at a constant rate (a basic and limiting assumption of the square-root of time analysis is linear flow at constant leakoff rate which gives a straight-line on the square-root of time plot). Since leakoff rate is usually not constant ("pressure-dependent")-a clear straight-line will not appear on the square-root of time plot. We therefore introduced a pressure transient analysis technique that uses the rate (leakoff)-normalized pressure change (pressure change divided by leakoff rate change) along with their derivatives to properly diagnose the linear flow regime. The leakoff rate is proportional to fracture compliance and the pressure change in the fracture. For log-log diagnostic purposes only, it is not necessary to calculate the compliance correctly (no fracture geometry estimate required), since leakoff-normalized pressure only requires the proportionality of leakoff rate and the first derivative of the pressure change [ $\Delta p = ISIP - P(t)$ ]:

$$q_L \sim d(\Delta p)/dt$$

The concept of leakoff-normalized pressure is equivalent to standard well testing superposition procedures when flow/injection rates vary. The main assumptions, of course, are that the fracture closes according to the laws of linear elasticity and maintains a constant area while closing.

As an example we show the analysis of Stress Test #1 - Injection #3 using various plotting techniques. Figure 57 shows that there is no half-slope straight-line on the log-log diagnostic

Appendix C. Use of Well Testing Diagnostic Plots to Determine Fracture Closure  
Pressure

plot. The derivative on the square-root of time plot (Figure 58) also shows that a straight-line is not present since the first derivative does not indicate constant slope. A straight-line can be drawn anywhere, which makes closure arbitrary. Figure 59 shows the leakoff-normalized plot. On this plot, half-slope can be detected for the first 1.5 minutes and closure is estimated at the end of linear flow at about 4,480 psi surface (0.90 psi/ft).

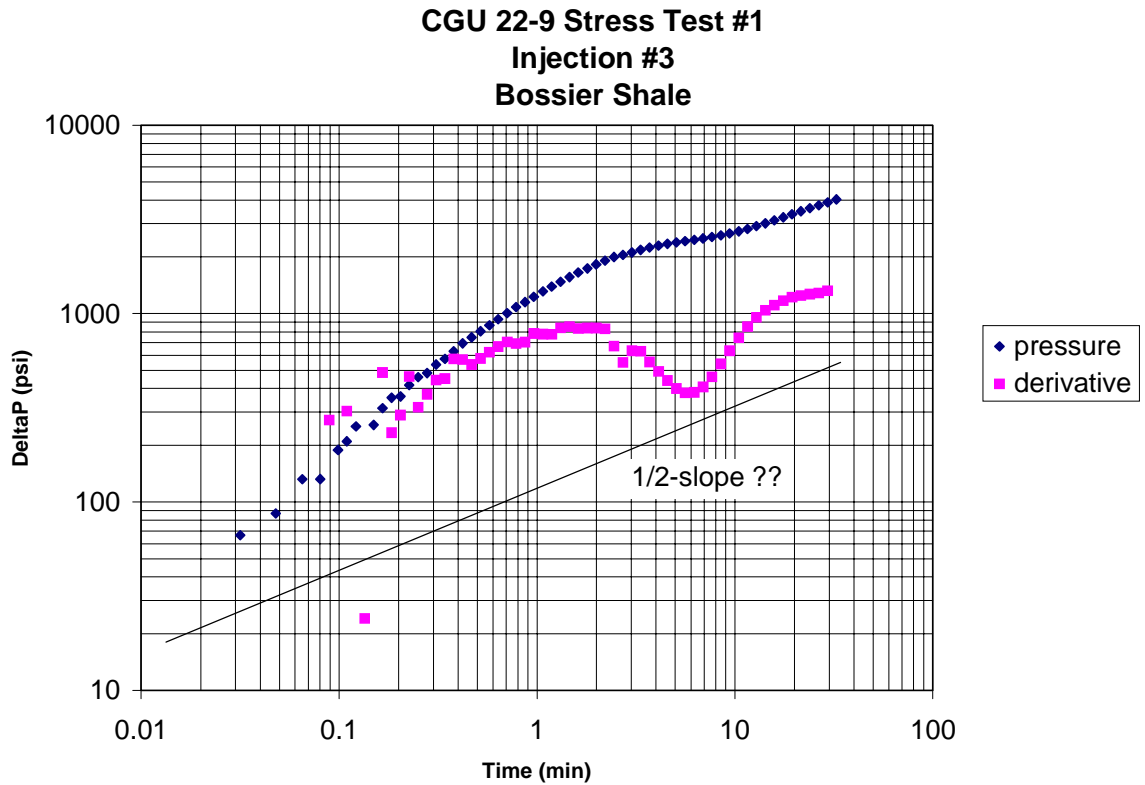


Figure 57. Log-log diagnostic plot

CGU 22-9 - Bossier Shale  
 Injection #3

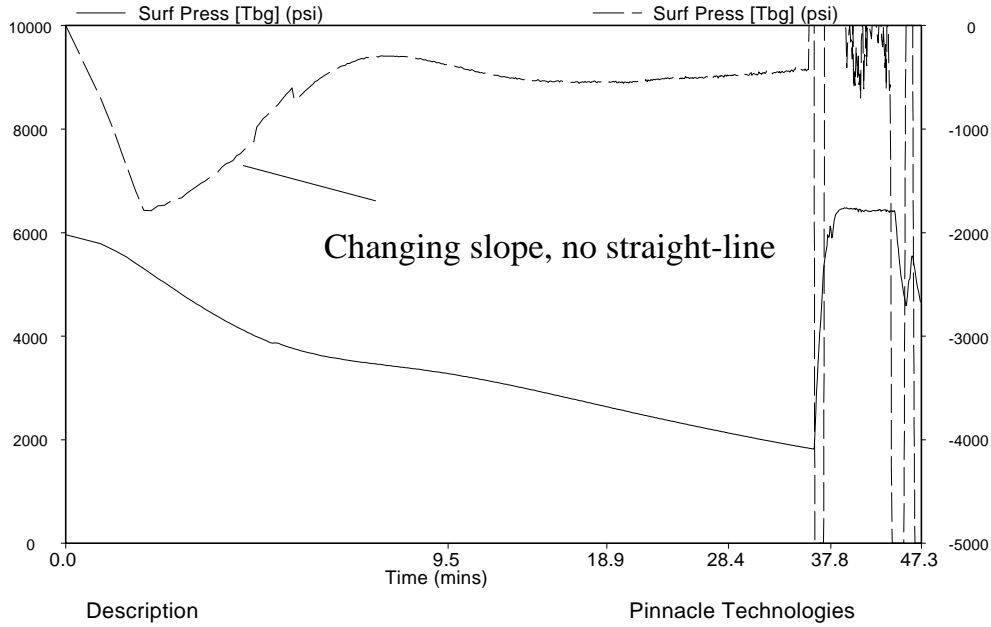


Figure 58. Square-root of time plot indicating no straight-line due to a varying derivative

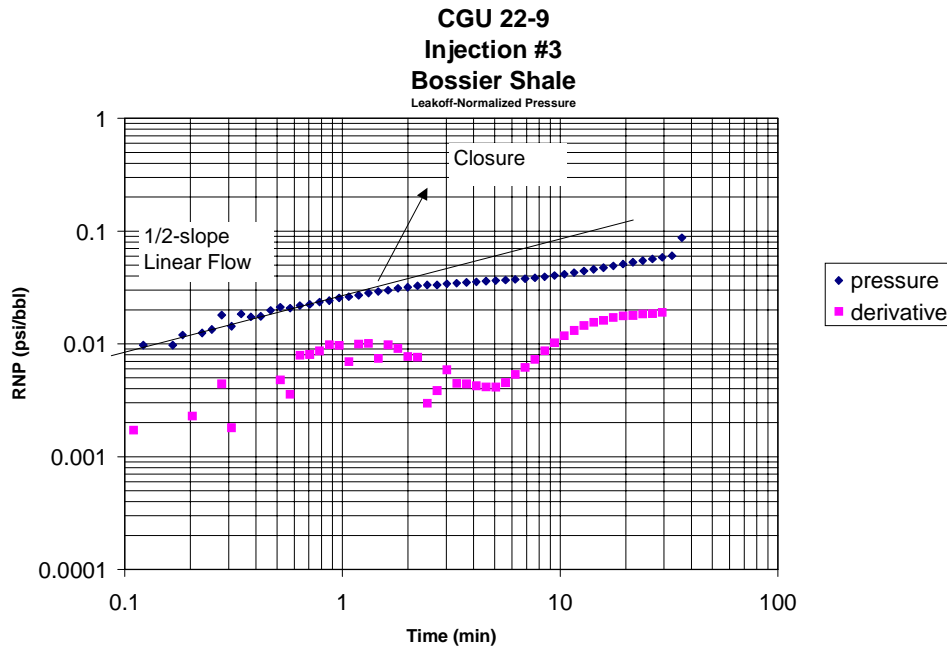


Figure 59. Leakoff-normalized diagnostic plot

## Appendix D. RA-Tracer Log and Production Log

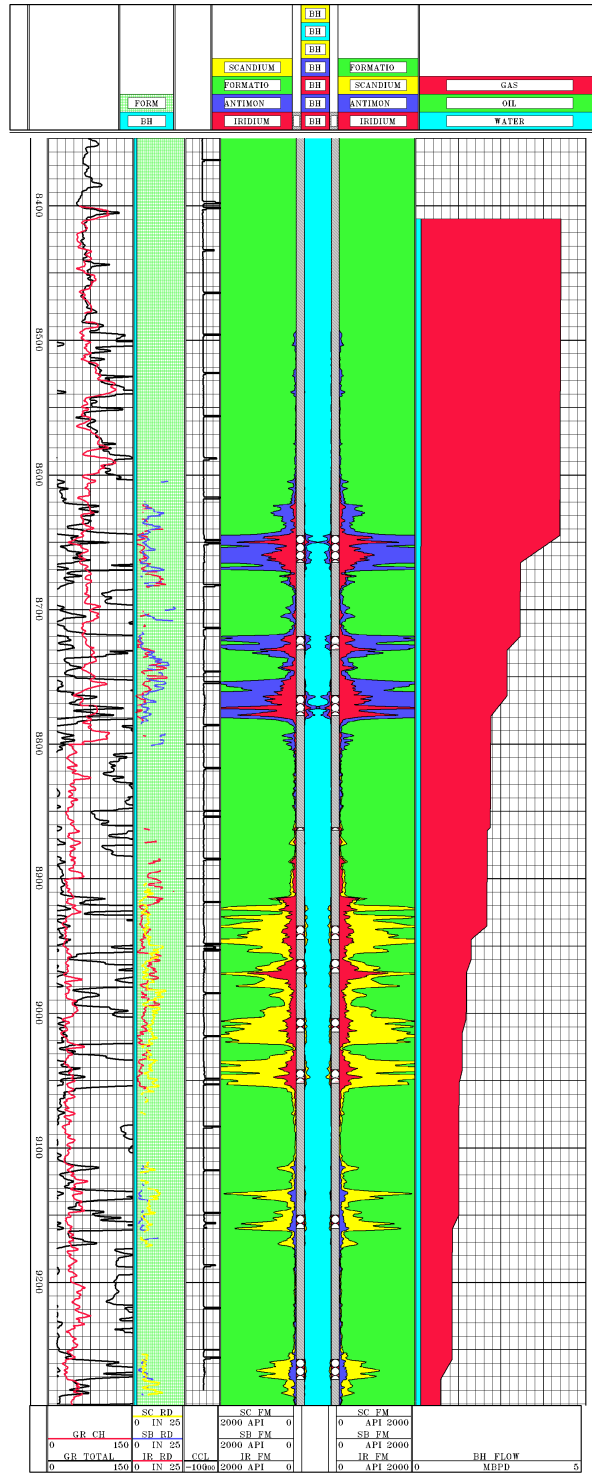


Figure 60. Tracer and Production Log: CGU 22-9

### Appendix E. Well Log CGU 22-9

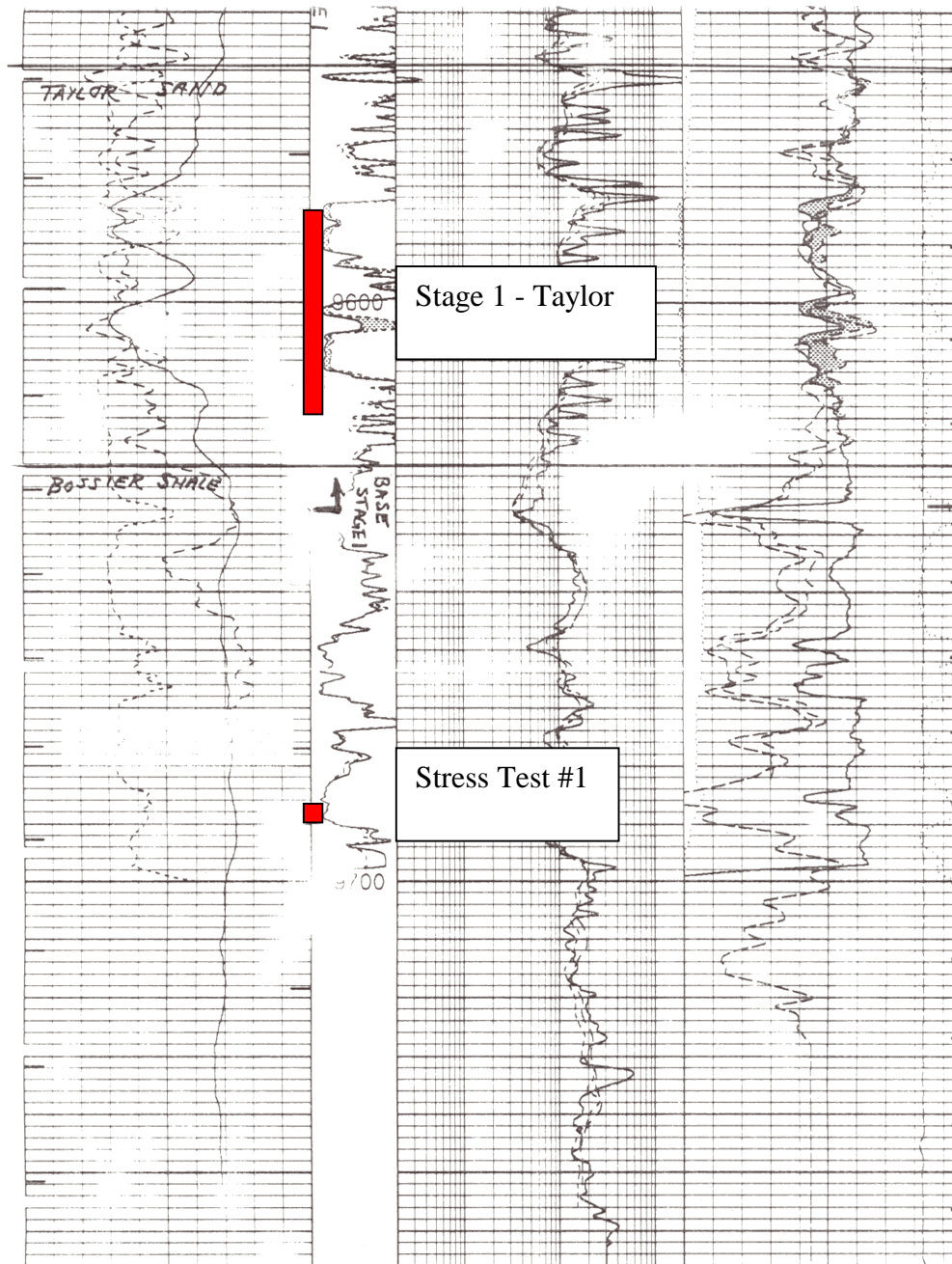


Figure 61. Stress Test #1 and Stage 1 – Taylor

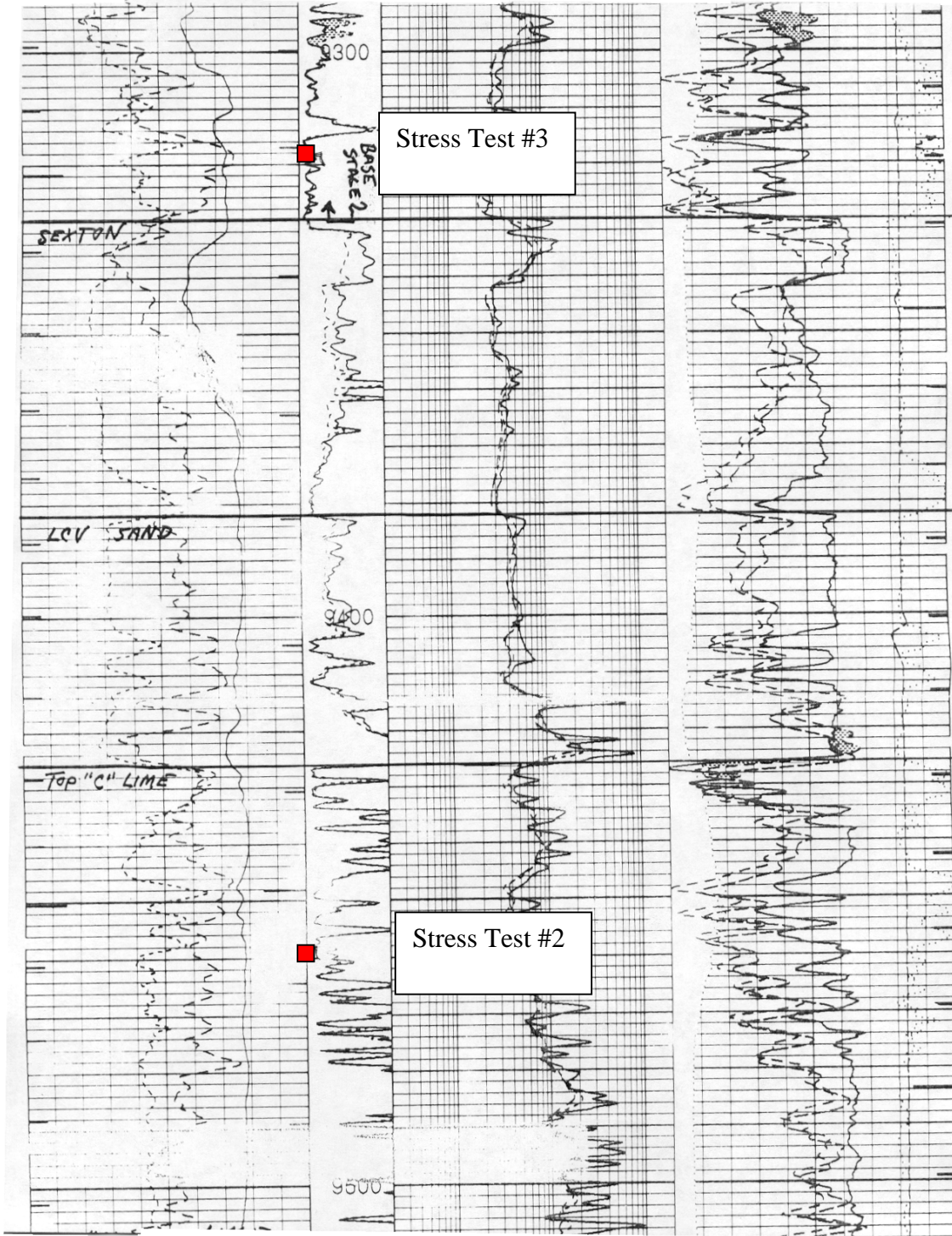


Figure 62. Stress Test #2 and #3

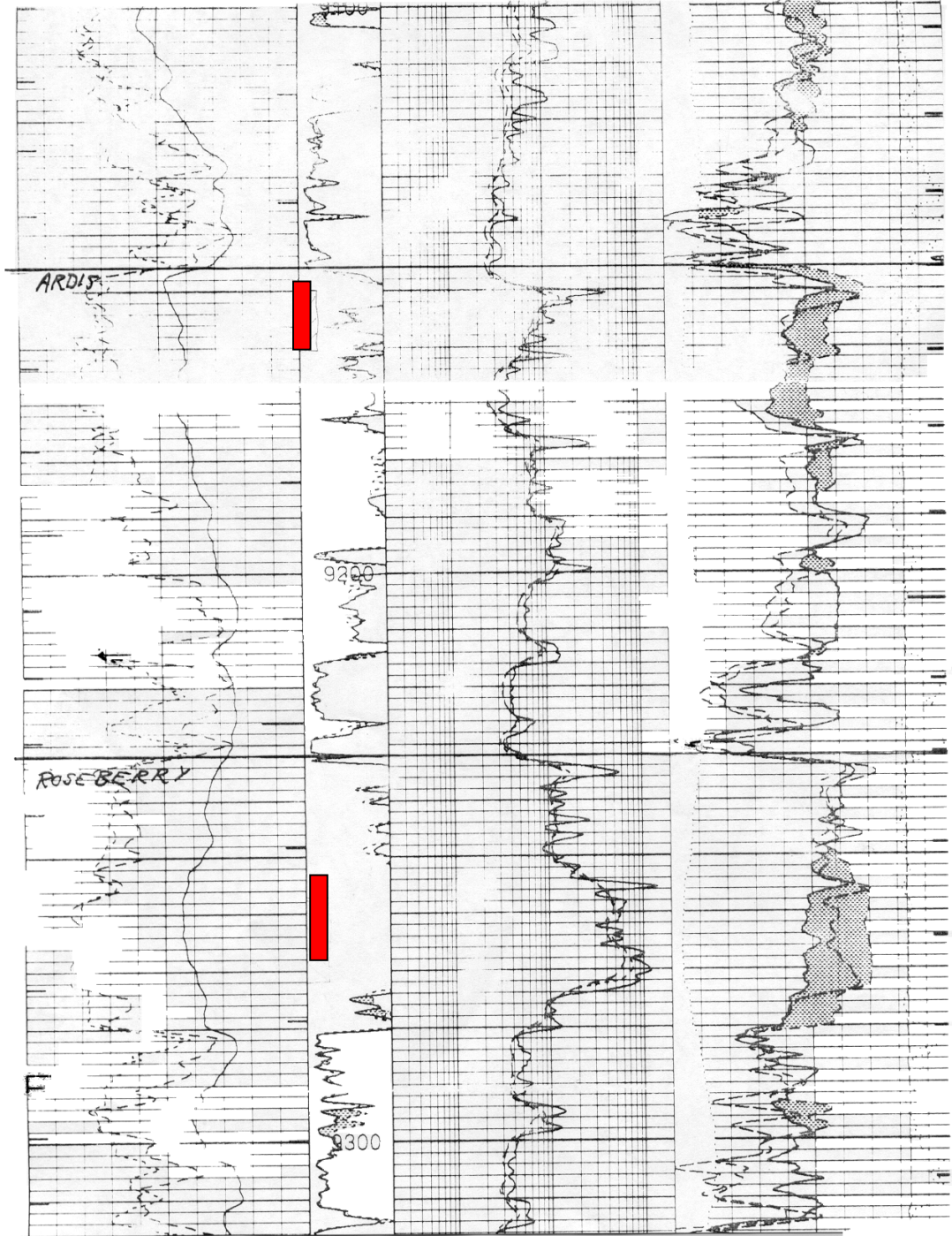


Figure 63. Stage #2 – Ardis and Roseberry Sands

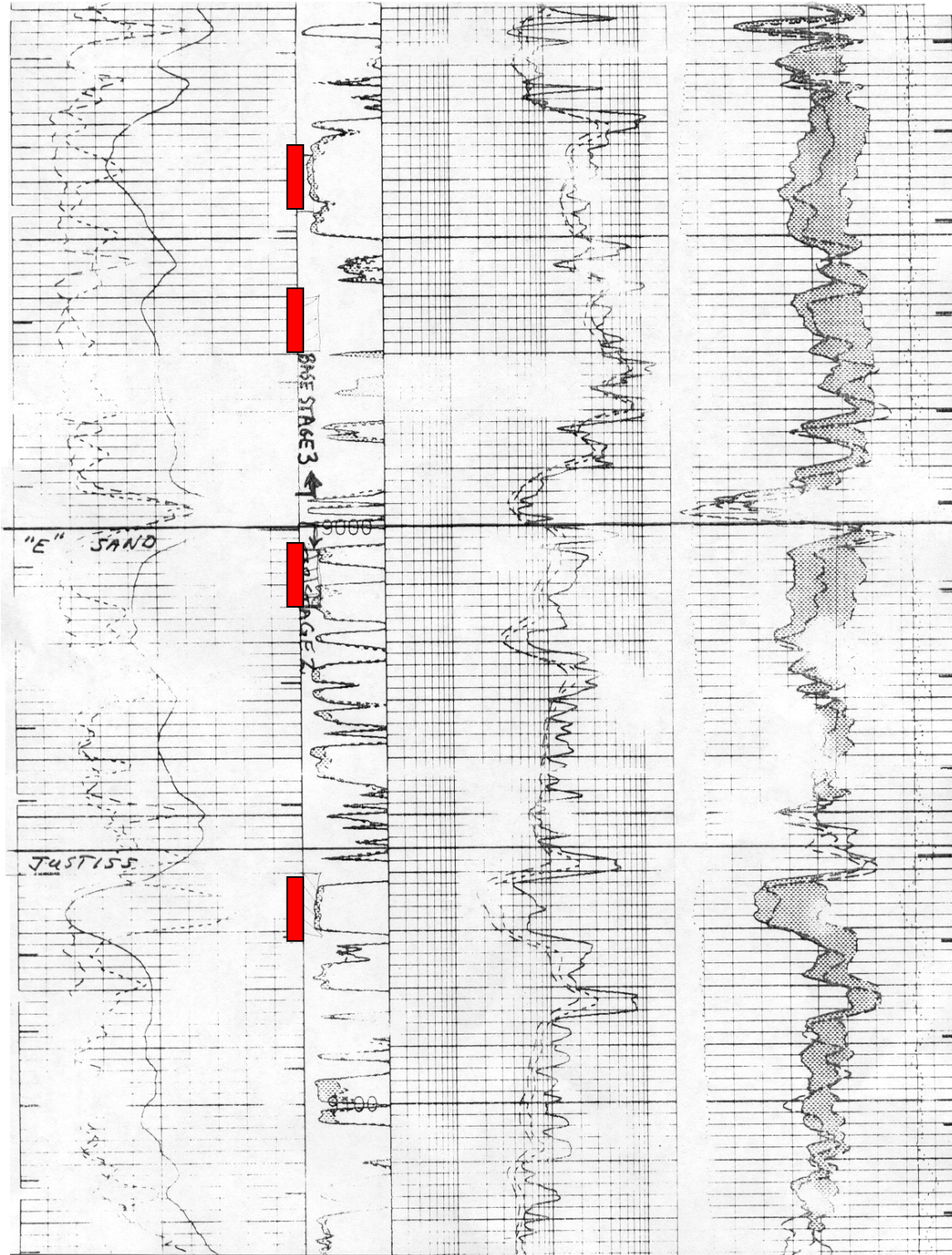


Figure 64. Stage #3 – “E” and Justice Sand

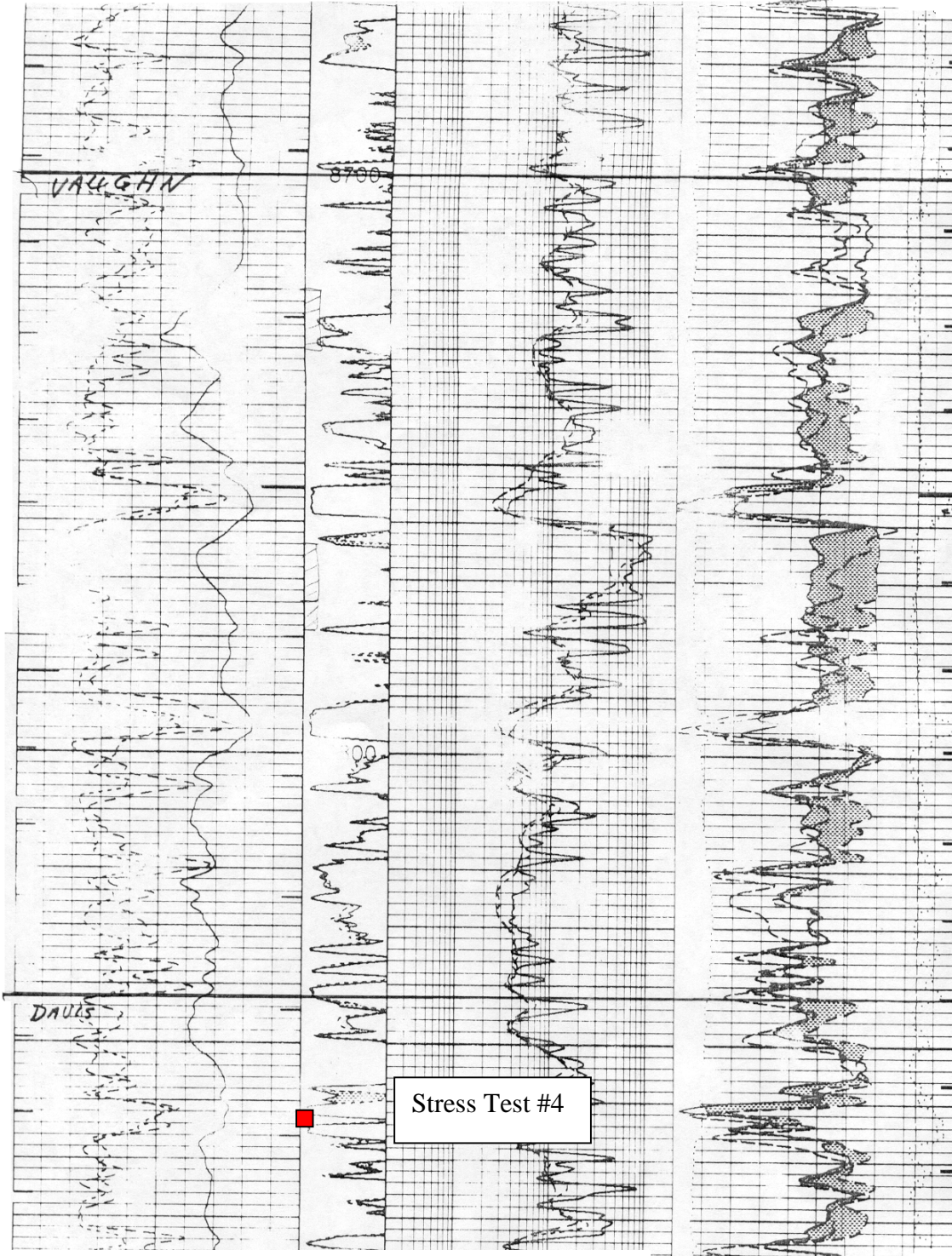


Figure 65. Stress Test #4 – Davis Sand/Shale

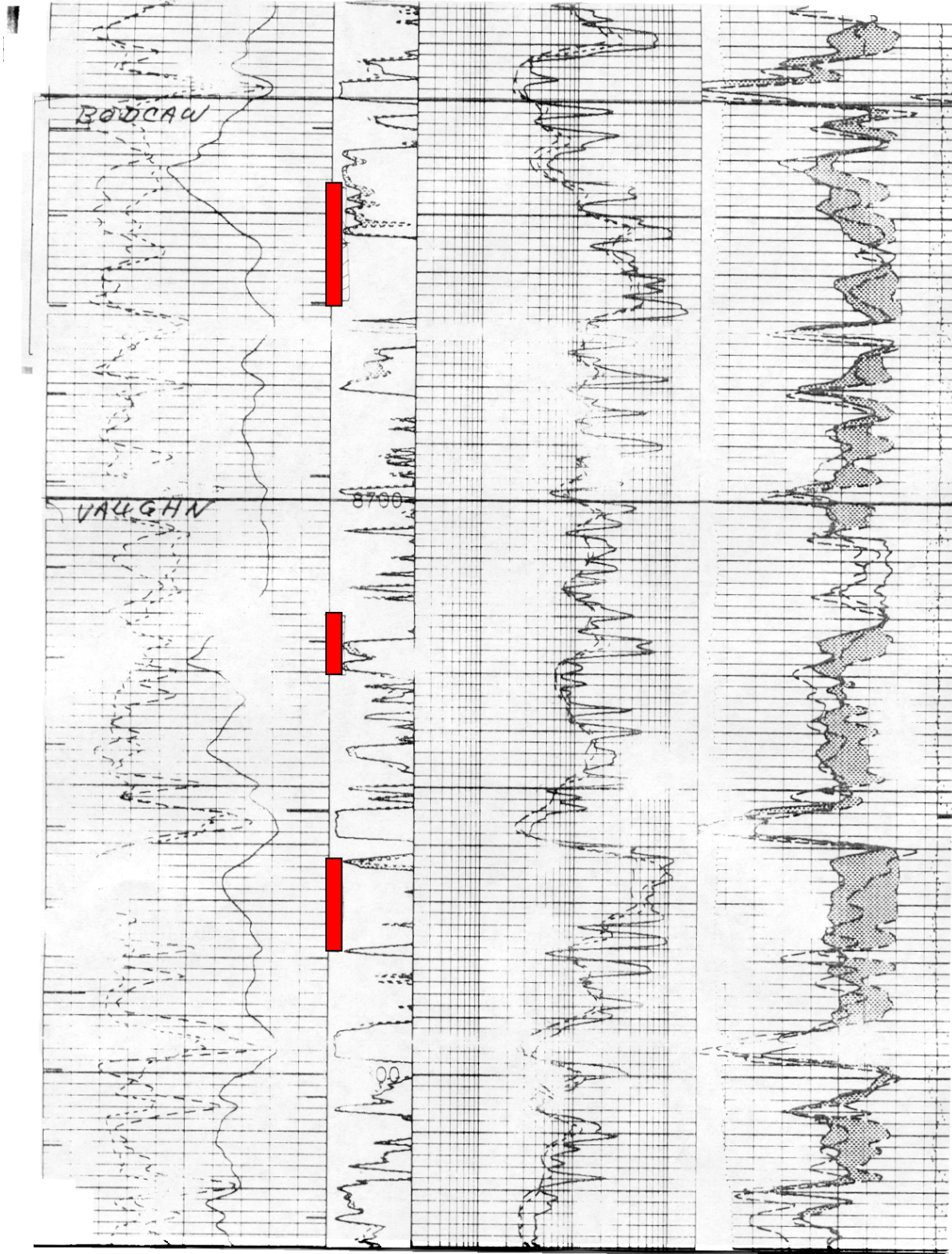


Figure 66. Stage #4 – Bodcaw and Vaughn Sands